Direct numerical simulation of Taylor–Couette flow with grooved walls: torque scaling and flow structure

Xiaojue Zhu[1,†], **Rodolfo Ostilla-Mónico**[1], **Roberto Verzicco**[1,2]
and Detlef Lohse[1,3]

[1]Physics of Fluids Group, MESA+ Institute and J. M. Burgers Centre for Fluid Dynamics, University of Twente, P.O. Box 217, 7500AE Enschede, The Netherlands

[2]Dipartimento di Ingegneria Industriale, University of Rome 'Tor Vergata', Via del Politecnico 1, Roma 00133, Italy

[3]Max-Planck Institute for Dynamics and Self-Organization, 37077 Göttingen, Germany

We present direct numerical simulations of Taylor–Couette flow with grooved walls at a fixed radius ratio $\eta = r_i/r_o = 0.714$ with inner cylinder Reynolds number up to $Re_i = 3.76 \times 10^4$, corresponding to Taylor number up to $Ta = 2.15 \times 10^9$. The grooves are axisymmetric V-shaped obstacles attached to the wall with a tip angle of $90°$. Results are compared to the smooth wall case in order to investigate the effects of grooves on Taylor–Couette flow. We focus on the effective scaling laws for the torque, flow structures, and boundary layers. It is found that, when the groove height is smaller than the boundary layer thickness, the torque is the same as that of the smooth wall cases. With increasing Ta, the boundary layer thickness becomes smaller than the groove height. Plumes are ejected from the tips of the grooves and secondary circulations between the latter are formed. This is associated with a sharp increase of the torque, and thus the effective scaling law for the torque versus Ta becomes much steeper. Further increasing Ta does not result in an additional slope increase. Instead, the effective scaling law saturates to the 'ultimate' regime effective exponents seen for smooth walls. It is found that even though after saturation the slope is the same as for the smooth wall case, the absolute value of torque is increased, and more so with the larger size of the grooves.

Key words: plumes/thermals, Taylor–Couette flow, turbulence simulation

---

1. Introduction

Non-smooth surfaces exist everywhere in nature, and many engineering applications need to deal with rough boundaries. The question of how local wall roughness affects global transport properties dates back to the pioneering study by Nikuradse (1933) in pipe flow. Nikuradse performed experiments on pipes with sand glued to the wall as densely as possible. The measurements of the friction coefficient $C_f = \tau/(\rho U^2/2)$,

† Email address for correspondence: xiaojue.zhu@utwente.nl

where τ is the surfaced averaged friction stress, ρ the fluid density and U the mean flow velocity, show that roughness has little impact in the laminar regime, but after increasing the Reynolds number Re, the friction factor turns upwards and reaches an asymptote. At the highest Re, the friction factor becomes independent of Re. Nikuradse then explained that, in the smooth case, the viscous sublayer depth depends on Re, and hence the friction factor. However, by introducing roughness, the viscous sublayer decreases down to the roughness scale, where the friction factor becomes independent of Re. Since then, there have been many studies concerning flow in pipes with surface roughness (see Jimenez (2004) for a review).

In general, studying the effect of a change of the boundary conditions at the wall will lead to a better understanding of the bulk–boundary layer (BL) interaction and the flow transport properties which are closely connected therewith. Next to pipe flow, the canonical systems in turbulent flows are Rayleigh–Bénard (RB) flow, in which a fluid is driven by the temperature difference between the hot bottom plate and cold top plate, and Taylor–Couette (TC) flow, in which a fluid is confined between two independently rotating coaxial cylinders. Both flows have been well studied and show rich patterns with smooth walls (see Ahlers, Grossmann & Lohse (2009) for a comprehensive review on RB flow and Fardin, Perge & Taberlet (2014); Grossmann, Lohse & Sun (2016) on TC flow). Eckhardt, Grossmann & Lohse (2007a,b) showed that pipe, RB and TC flows are analogous to each other. Because of the close analogy, a better understanding of TC flow will lead to a more profound insight also in RB and pipe flow, and vice versa.

The temperature difference between the top and bottom plate in RB flow is analogous to different rotation rates of the inner and outer cylinders in TC flow. The rotation difference in TC flow is non-dimensionally characterized by the Taylor number Ta, which is analogous to the dimensionless temperature difference in RB flow, i.e. the Rayleigh number Ra. For TC flow, the global transport property is expressed as the dimensionless torque Nu_ω, which is analogous to the dimensionless heat flux in RB flow, i.e. the Nusselt number Nu. In TC flow, when the driving force Ta is small, both the BL and the bulk are of laminar type. When increasing Ta, first the bulk becomes turbulent, and finally also the BLs (Grossmann, Lohse & Sun 2014; Ostilla-Mónico *et al.* 2014a,b). This state is the so-called 'ultimate' regime. The ultimate regime is relevant not only conceptually (Kraichnan 1962; Grossmann & Lohse 2000, 2001), but also because many applications in nature and engineering are within that regime. For TC flow, the BL transition was first found by Lathrop, Fineberg & Swinney (1992a,b) and Lewis & Swinney (1999), though they did not relate it to the 'ultimate' regime. Later, van Gils *et al.* (2011), Huisman *et al.* (2012, 2013) and Ostilla-Mónico *et al.* (2014a,b) put it into this conceptual framework. In RB turbulence, the ultimate regime was experimentally found by He *et al.* (2012a,b). In both RB and TC turbulence, the ultimate regime scalings, namely $Nu \sim Ra^\beta$ in RB flow and $Nu_\omega \sim Ta^\beta$ in TC flow, have an effective exponent of $\beta \approx 0.38$–0.40, originating from $1/2$ (Kraichnan 1962) and logarithmic corrections (Grossmann & Lohse 2011, 2012).

For RB flow with roughness, various different effective scaling laws relating heat transport to the driving, written in the form $Nu = ARa^\beta$, were suggested. When the height of roughness δ is larger than the thermal BL thickness $\lambda_\theta \simeq L/(2Nu)$, where L is the distance between two plates, Shen, Tong & Xia (1996) found that the prefactor A increased by 20 %, whereas the exponent β did not change on using rough surfaces made of regularly spaced pyramids. Later, by using the same facility, but a different pyramid height (9 mm compared to 3.2 mm in Shen *et al.* (1996)), Du & Tong

(2000) measured the increase of A to be as much as 76 % and the exponent β again stayed the same. Based on flow visualization, Du & Tong (2000) concluded that the enhancement of heat transport is due to plume ejection from the tip of the pyramids. Also Ciliberto & Laroche (1999) found that β was unaffected but, more surprisingly, A decreased when $\lambda_\theta < \delta$. In another experiment, which used pyramid roughness, by Qiu, Xia & Tong (2005), both A and β were found to increase and the new β with roughness was 0.35. Wei *et al.* (2014) found $\beta \approx 0.35$ with roughness on both the lower and upper plates. In contrast, Stringano, Pascazio & Verzicco (2006), who numerically investigated RB convection over grooved plates, showed that the secondary vortex inside the grooves would lift up the BL and help the plumes detach from the tip, which is consistent with the result of Du & Tong (2000). Both A and β increased and β changed to approximately 0.37. By implementing V-shaped axis-symmetrical roughness both on the sidewalls and horizontal plates, Roche *et al.* (2001) obtained an increase of β to approximately 0.51, which was interpreted as triggering the ultimate region $1/2$ law without the logarithmic correction proposed by Kraichnan (1962), after λ_θ drops below the roughness height. They concluded that the roughness imposes a new length scale on the thermal BLs. They argued that the sublayer thickness would be fixed by the roughness such that the logarithmic correction would become irrelevant. Ahlers *et al.* (2009) pointed out that the $1/2$ scaling observed might possibly be due to a crossover between rough surfaces from a regime with a groove depth less than the BL thickness to a regime where the groove depth is larger than the BL thickness. Tisserand *et al.* (2011) postulated that, if this interpretation was correct, then the $\beta = 1/2$ behaviour of RB flow with roughness would be fortuitous. Salort *et al.* (2014) further showed that, in their model, β could range from 0.38 to 0.5, depending on the extent of instability of the BL. Clearly, more work is needed to resolve this issue.

We now come to TC flow with roughness, the subject of the present study, for which studies are less common. Cadot *et al.* (1997) performed experiments with equidistant ribs on both the inner and the outer surface. These ribs were straight and parallel to the axis of the cylinders. With smooth boundaries, the dissipation in the boundary is dominant and the drag coefficient decreases with increasing Re. However, with rough walls, Cadot *et al.* (1997) argued that the dissipation in the BLs is no longer dominant, due to the extra dissipation in the bulk. In that regime the global drag coefficient becomes constant with increasing Re. Inspired by this work, van den Berg *et al.* (2003) performed further experiments with the same style of roughness. They reported results for the four cases of two smooth walls, smooth-inner/rough-outer, rough-outer/smooth-inner, and two rough walls. The data were interpreted within the Grossmann–Lohse (GL) theory (Grossmann & Lohse 2000, 2001, 2002). The flow was found to change from BL dominant to bulk dominant. In the case with two rough walls, the drag coefficient is again found to be independent of Re. The phenomenon of drag saturation with increasing Re is very similar to that found by Nikuradse (1933) in his rough pipe experiments.

We stress that there are usually two different types of wall roughness. In the first type the roughness is arranged in such a way as to impede the mean flow. We call this 'perpendicular roughness'. This kind of roughness element seems to be a more efficient generator of skin friction than smooth walls (Jimenez 2004). The studies of Cadot *et al.* (1997) and van den Berg *et al.* (2003) can both be included in this category. The other possibility is to arrange the roughness aligned with the mean flow, i.e. 'parallel roughness'. A well-documented example is the flow over riblets (Choi, Moin & Kim 1993; Chu & Karniadakis 1993). Under specific circumstances they decrease
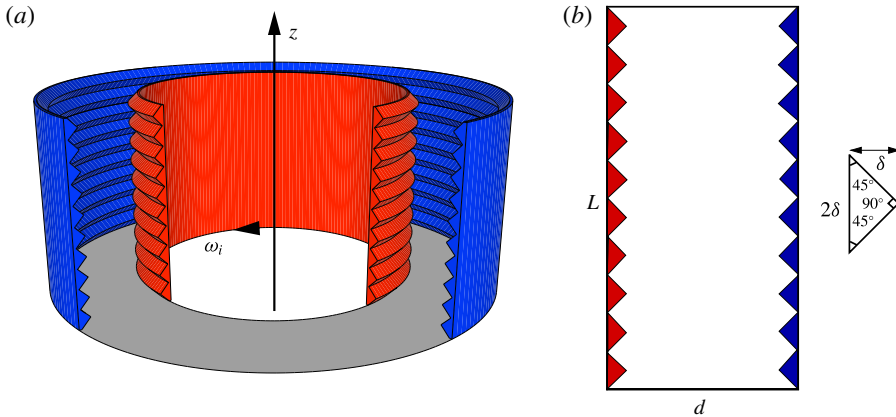
FIGURE 1. (Colour online) Schematic view of the Taylor–Couette system and the groove geometry. (*a*) Three-dimensional view. The inner cylinder with radius r_i is rotating with angular velocity ω_i. The outer cylinder with radius r_o is at rest. (*b*) Cross-section view of the gap between the cylinders: $d = r_o - r_i$. The length scale of the grooves is δ.

drag by 6 % (Choi *et al.* 1993). Many different kinds of roughness can be formed by combining these two approaches.

Inspired by the above studies, especially the similarities between pipe, RB and TC flow, we study how the Nu_ω versus Ta scaling and the corresponding flow structure behave with roughness in TC. In the present study, we perform direct numerical simulation (DNS) of TC flow with grooved walls. Because the grooves are quite large compared to the viscous scale, we avoid calling them roughness, similar to Stringano *et al.* (2006). The grooves implemented here are V-shaped obstacles attached to the wall with a tip angle of 90° and axisymmetric to the axis of cylinder. This arrangement of grooves is categorized as parallel roughness. A schematic view of the structure is shown in figure 1. Note that the rough element type in this study is similar to the one used in Stringano *et al.* (2006), but different from the one used in Shen *et al.* (1996) and Du & Tong (2000), in which pyramid structures were used.

Our motivations are as follows: (i) DNS provides us with the ability to reproduce all the details of the flow field which are unavailable in experiments, and therefore enables us to reveal the connection between the effective scaling laws for the torque, the boundary layer, and the flow structures. (ii) We want to answer the question whether, with parallel roughness, the ultimate regime effective scaling exponent β would change, or whether it stays the same as in the smooth case, namely $\beta = 0.38$ in the relevant Ta regime.

The manuscript is organized as follows. In §2, we describe the numerical methods and parameter settings. In §3, we show the effective scaling laws between the Nusselt number and Taylor number in smooth and grooved cases. In §4, it is shown how grooves change the flow structure. Section 5 presents the boundary layer dynamics with grooves. Finally, conclusions are drawn in §6.

2. Numerical settings

2.1. *Parameter descriptions*

In the present study, the outer cylinder is stationary and only the inner cylinder is rotating and thus driving the flow. The flow is bounded by two lateral grooved walls

cylinders with no-slip boundary conditions. The lower and upper surfaces are replaced by axially periodic boundary conditions and therefore do not include the effects of end walls unavoidably present in TC experiments. The grooves of the lateral walls are V-shaped, with a tip angle of 90° and a height δ (figure 1). r_i and r_o are the base radii of the inner and the outer cylinder without grooves, respectively. The valley-to-valley distance $d = r_o - r_i$ is used to non-dimensionalize all lengths and the base velocity of the inner cylinder $U = r_i\omega_i$ for normalizing velocities, where ω_i is the angular velocity of the inner cylinder. The inner grooves rotate with the inner cylinder, and thus have constant angular velocity. This means that the azimuthal velocity at the tip of the groove is slightly larger by a factor of $(r_i + \delta)/r_i$ than the velocity at the valley of the inner cylinder. The geometry of the system is fixed at a specific radius ratio $\eta = r_i/r_o = 0.714$. The reasons for keeping the outer cylinder stationary and choosing such a radius ratio are because they are close to the previous experimental and numerical studies (Lathrop *et al.* 1992*a*,*b*; Lewis & Swinney 1999; Huisman *et al.* 2012, 2013; Ostilla-Mónico *et al.* 2014*a*), so that we can make direct comparisons with those results. We define the dimensionless radial coordinate as $y = (r - r_i)/d$, so that it ranges from 0 at the inner cylinder to 1 at the outer cylinder. Brauckmann & Eckhardt (2013) and Ostilla-Mónico *et al.* (2014*a*,*b*) showed that a rotational symmetry of order six does not change the flow statistics for $\eta = 0.714$. We follow their approach and choose this value to reduce the number of grids and the computational cost. The aspect ratio Γ is chosen to be $\Gamma = L/d = 2\pi/3 = 2.094$ (Ostilla-Mónico *et al.* 2014*a*), where L is the axial domain length. In this way one pair of Taylor vortices can be sustained in our DNS. The dimensionless torque is defined in the form $Nu_\omega = T/T_{pa}$, where T_{pa} is the torque of the purely azimuthal laminar state without grooves.

The motion of the fluid is governed by the incompressible Navier–Stokes equations

$$\frac{\partial \boldsymbol{u}}{\partial t} + \boldsymbol{u} \cdot \nabla \boldsymbol{u} = -\nabla p + \frac{f(\eta)}{Ta^{1/2}} \nabla^2 \boldsymbol{u}, \tag{2.1}$$

$$\nabla \cdot \boldsymbol{u} = 0, \tag{2.2}$$

where $\boldsymbol{u}$ and p are the fluid velocity and pressure, respectively. $f(\eta)$ is a geometrical factor which is in the form

$$f(\eta) = \frac{(1+\eta)^3}{8\eta^2}. \tag{2.3}$$

The *Ta* number, in the absence of outer cylinder rotation, is written as

$$Ta = \frac{1}{64} \frac{(1+\eta)^4}{\eta^2} d^2 (r_i + r_o)^2 \omega_i^2 \nu^{-2}, \tag{2.4}$$

where ν is the kinematic viscosity of the fluid.

An alternative way to determine the system by using the inner cylinder Reynolds number $Re_i = r_i\omega_i d/\nu$, rather than the *Ta* number, is suggested in the work of Lathrop *et al.* (1992*a*,*b*), Lewis & Swinney (1999). Note that these two definitions can be easily translated into each other using the relation

$$Ta = [f(\eta)Re_i]^2. \tag{2.5}$$

2.2. *Numerical method*

A second-order finite difference code is employed for the present research, which is written in cylindrical coordinates and discretized on a staggered mesh. Details of the base code can be found in Verzicco & Orlandi (1996) and van der Poel *et al.* (2015*a*). The code has been extensively validated in Ostilla *et al.* (2013) and Ostilla-Mónico *et al.* (2014*a*,*b*). Time marching is performed by a third-order Runge–Kutta scheme and the fractional step is used for the pressure–momentum coupling, in combination with a semi-implicit scheme for viscous terms. To achieve large-scale computation, a hybrid MPI-pencil and OpenMP decomposition is used to parallelize the code.

An immersed boundary (IB) technique (Fadlun *et al.* 2000) has been implemented into the code in order to deal with grooves on the surfaces of both cylinders. The main idea of the IB method is to add a body force term f to the momentum equation (2.1), mimicking the boundary effect, to enforce in this way the desired velocity on the boundary, so that a regular non-body fitted mesh can be used. The information transfer between boundaries and nearby meshes is performed by means of interpolation. The advantage of the IB method is immediate: flow bounded by arbitrary complex geometry can be easily solved on a very simple mesh with an additional body force. This IB method has already been validated in a variety of contexts (Fadlun *et al.* 2000; Stringano *et al.* 2006). For more details on the implementation, accuracy and application of the IB method, we refer the reader to Fadlun *et al.* (2000) and Mittal & Iaccarino (2005).

In order to guarantee the proper resolution, we proceed as follows. The mean angular velocity current J^ω, defined by

$$J^\omega = r^3(\langle u_r \omega \rangle_{A,t} - \nu \partial_r \langle \omega \rangle_{A,t}), \tag{2.6}$$

is strictly conserved along the radius r (Eckhardt *et al.* 2007*b*). In this equation, u_r denotes the radial velocity component and ω the angular velocity. On the one hand, J^ω is related to the torque T by $T/(2\pi L \rho_f) = J^\omega$, where ρ_f is the fluid density. On the other hand, J^ω can also be related to Nu_ω as $Nu_\omega = T/T_{pa} = J^\omega/J_0^\omega$, in which J_0^ω is the angular velocity current of the purely azimuthal state without grooves. $\langle \cdots \rangle_{A,t}$ represents averages over a cylindrical surface at radius r and over time. Numerically, J^ω will deviate slightly from being constant due to numerical errors. To quantify this difference, we define

$$\Delta_J = \frac{\max(J^\omega(r)) - \min(J^\omega(r))}{\langle J^\omega(r) \rangle_r}, \tag{2.7}$$

where the maximum and minimum are determined over all r, which is chosen to be within the range $r_i + \delta \leqslant r \leqslant r_o - \delta$ because of the influences of the grooves. As illustrated by Ostilla *et al.* (2013), $\Delta_J \leqslant 0.01$ is a very strict requirement for the meshes. We make sure that all of our simulations meet this criterion (see table 1). An additional issue on resolution within the near-wall region by using the IB method is that grooves do not coincide with the coordinate lines. This results in a finer mesh in the radial and axial directions. Compared to the case without grooves at the same *Ta* number, the number of grids increases by at least by a factor of four. Figure 2 shows an example of the mesh in the meridional plane.
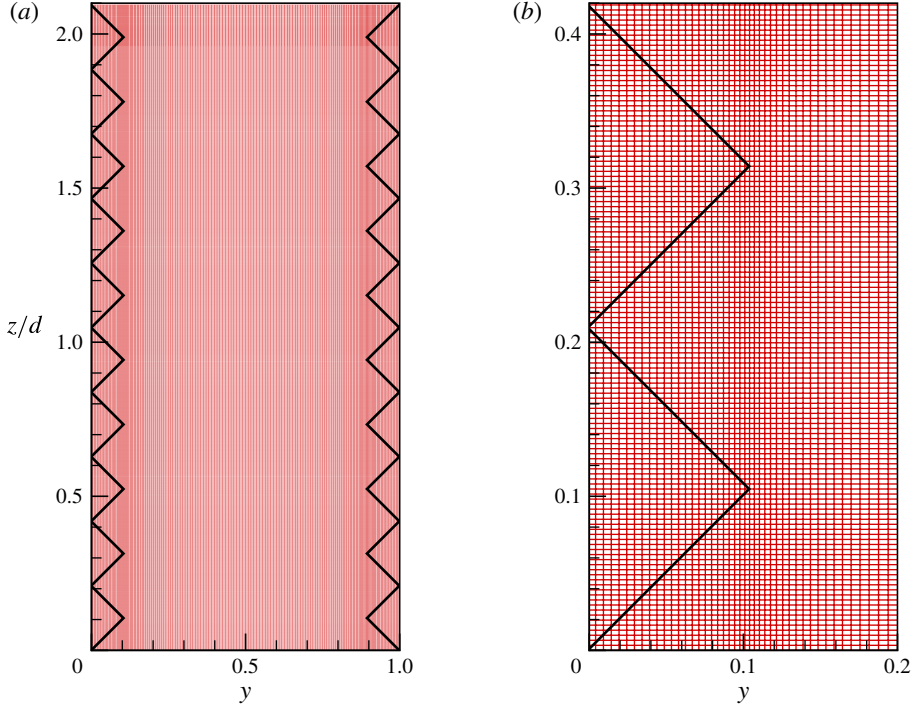
FIGURE 2. (Colour online) An example of the mesh used in our simulations in the meridional plane with radial grids and axial grids of $N_r \times N_z = 160 \times 512$. (*a*) Whole surface. (*b*) Enlargement of the region near the grooves. A more refined mesh is needed near the tip of the grooves. Note that the grid resolution in the axial direction is much higher than the one used in Ostilla *et al.* (2013), Ostilla-Mónico *et al.* (2014*a*) because here we have to implement the IB method.

2.3. *Explored phase space*

Inspired by the literature on RB flow with roughness (Shen *et al.* 1996; Du & Tong 2000), in which it was found that the heat flux increase can not be explained solely by the increase of surface area, three different groove heights with the same total area in each series, i.e. $\delta = 0.052d$, $\delta = 0.105d$ and $\delta = 0.209d$, corresponding to 20, 10 and 5 grooves on both surfaces of cylinder, were analysed. In each series with the same groove height, *Ta* is varied from 10^5 to 10^9. We then directly compare our results with our previous simulations by Ostilla *et al.* (2013) and Ostilla-Mónico *et al.* (2014*a*), as well as experiments by Lewis & Swinney (1999), all without grooves. The details of all simulations are given in table 1.

3. Global response: dimensionless torque

As mentioned above, the global response of transport of the TC system can be expressed as the torque which is required to keep the inner cylinder at a fixed angular velocity. To investigate the effect of the grooved walls, in this section, the dimensionless torque Nu_ω is presented as a function of *Ta*, i.e. $Nu_\omega = ATa^\beta$, with grooved walls, in comparison with the results for smooth walls.

Figure 3 shows Nu_ω with increasing *Ta* for smooth cases and grooved cases with three series of different groove heights. For the smooth TC flow, from $Ta = 2.5 \times 10^5$

δ/d	Ta	Re_i	$N_\theta \times N_r \times N_z$	Nu_ω	$100\Delta_J$
0.052	2.44×10^5	4.00×10^2	$64 \times 160 \times 512$	2.869	0.21
0.052	7.04×10^5	6.80×10^2	$64 \times 160 \times 512$	3.655	0.42
0.052	1.91×10^6	1.12×10^3	$64 \times 192 \times 768$	4.678	0.33
0.052	3.90×10^6	1.60×10^3	$128 \times 224 \times 896$	5.535	0.26
0.052	9.52×10^6	2.50×10^3	$128 \times 256 \times 1024$	6.646	0.41
0.052	2.39×10^7	3.96×10^3	$160 \times 320 \times 1280$	7.208	0.38
0.052	4.77×10^7	5.60×10^3	$160 \times 400 \times 1600$	8.421	0.62
0.052	9.75×10^7	8.00×10^3	$192 \times 512 \times 2048$	11.11	0.56
0.052	2.15×10^8	1.19×10^4	$192 \times 512 \times 2048$	16.60	0.82
0.052	4.62×10^8	1.74×10^4	$256 \times 640 \times 2560$	22.70	0.79
0.052	9.75×10^8	2.53×10^4	$256 \times 640 \times 2560$	30.85	0.83
0.052	2.15×10^9	3.76×10^4	$384 \times 700 \times 2800$	41.12	0.78
0.105	2.44×10^5	4.00×10^2	$64 \times 160 \times 512$	2.907	0.10
0.105	7.04×10^5	6.80×10^2	$64 \times 160 \times 512$	3.653	0.26
0.105	1.91×10^6	1.12×10^3	$64 \times 192 \times 768$	4.450	0.32
0.105	3.90×10^6	1.60×10^3	$128 \times 256 \times 1024$	5.151	0.31
0.105	9.52×10^6	2.50×10^3	$128 \times 256 \times 1024$	6.096	0.28
0.105	2.39×10^7	3.96×10^3	$160 \times 384 \times 1536$	7.933	0.49
0.105	4.77×10^7	5.60×10^3	$160 \times 400 \times 1600$	11.15	0.37
0.105	9.75×10^7	8.00×10^3	$192 \times 512 \times 2048$	15.24	0.68
0.105	2.15×10^8	1.19×10^4	$192 \times 512 \times 2048$	20.32	0.42
0.105	4.62×10^8	1.74×10^4	$256 \times 640 \times 2560$	26.56	0.83
0.105	9.75×10^8	2.53×10^4	$256 \times 640 \times 2560$	34.76	0.57
0.209	1.03×10^5	2.60×10^2	$64 \times 160 \times 512$	2.452	0.19
0.209	2.44×10^5	4.00×10^2	$64 \times 160 \times 512$	3.333	0.24
0.209	7.04×10^5	6.80×10^2	$64 \times 160 \times 512$	4.516	0.39
0.209	1.91×10^6	1.12×10^3	$64 \times 192 \times 768$	5.364	0.23
0.209	3.90×10^6	1.60×10^3	$128 \times 256 \times 1024$	6.489	0.47
0.209	9.52×10^6	2.50×10^3	$128 \times 256 \times 1024$	8.016	0.59
0.209	2.39×10^7	3.96×10^3	$160 \times 384 \times 1536$	11.73	0.63
0.209	4.77×10^7	5.60×10^3	$160 \times 400 \times 1600$	14.15	0.48
0.209	9.75×10^7	8.00×10^3	$192 \times 512 \times 2048$	17.93	0.72
0.209	2.15×10^8	1.19×10^4	$192 \times 512 \times 2048$	22.49	0.61

TABLE 1. Values of the control parameters and the numerical results of the simulations. Three series of different groove height are presented. In each series, we vary Ta, and thus Re_i. The fourth column shows the number of grids used in the azimuthal (N_θ), radial (N_r) and axial direction (N_z). The fifth column shows the dimensionless torque, Nu_ω. The last column shows the criteria of resolution we choose, i.e. angular velocity current difference along the radius J_ω. All of the simulations were run in a reduced geometry with $L = 2\pi/3$ and a rotation symmetry of the order 6. The corresponding cases at the same Ta without grooves (with smooth cylinders) can be found in Ostilla *et al.* (2013), Ostilla-Mónico *et al.* (2014a).

up to $Ta = 3 \times 10^6$, an effective scaling law of $Nu_\omega \sim Ta^{1/3}$ is found, which is associated with the laminar Taylor vortices. Between $Ta = 3 \times 10^6$ and $Ta = 2 \times 10^8$, there is a transitional region in which first the bulk becomes turbulent, and then the boundary layers also become gradually turbulent (see the gradually growing turbulent BL in Ostilla-Mónico *et al.* (2014a)). When Ta is even larger, the flow is fully
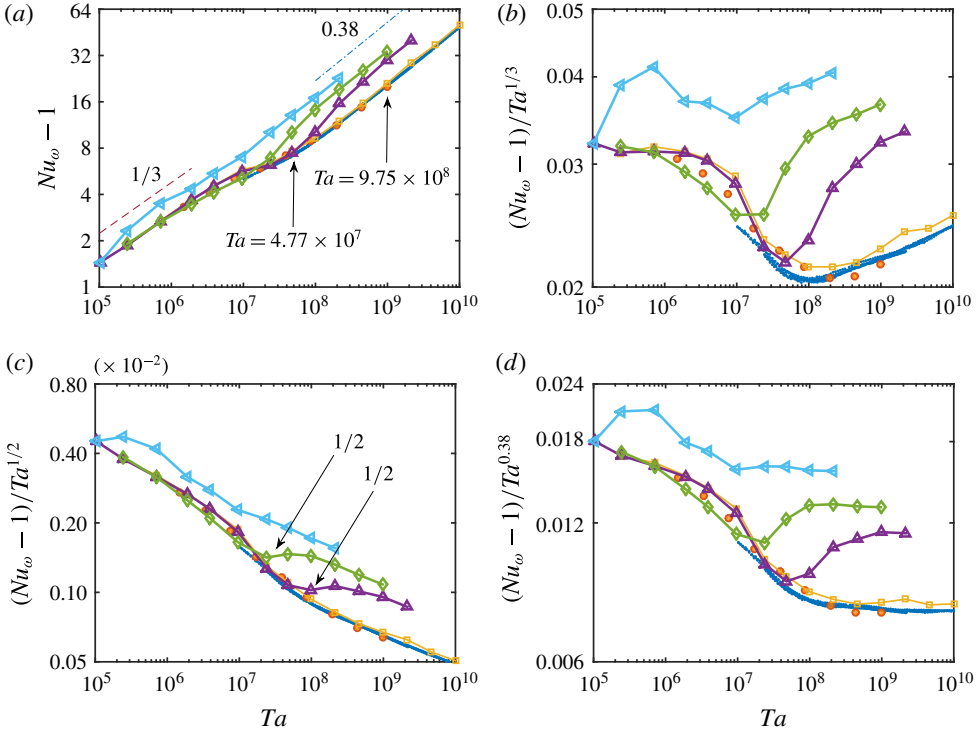
FIGURE 3. (Colour online) (*a*) Nusselt number as function of *Ta* for $\eta = 0.714$. The data are from experiments and numerical simulations: $\cdots$, smooth walls experiments by Lewis & Swinney (1999); $\bigcirc$, smooth walls simulations by Brauckmann & Eckhardt (2013); $\square$, smooth walls simulations by Ostilla-Mónico *et al.* (2014a); $\triangle$, grooved walls simulations with $\delta = 0.052d$ in the present study; $\diamondsuit$, grooved walls simulations with $\delta = 0.105d$ in the present study; $\triangleleft$, grooved walls simulations with $\delta = 0.209d$ in the present study. Dashed line and dotted dashed line show the 1/3 and the 0.38 slope. Two arrows indicate $Ta = 4.77 \times 10^7$ and $Ta = 9.85 \times 10^8$ in the $\delta = 0.105d$ series. The former *Ta* is in the regime where the scaling slope is larger than 0.38 and the latter is in the regime where the slope saturates back to 0.38. These two cases are used in the main text as examples to show why Nu_ω is increased and why the scaling slope is changed. (*b*) The same as (*a*), but now the Nusselt number is scaled with $Ta^{-1/3}$. (*c*) The same as (*a*), now with the Nusselt number scaled with $Ta^{-1/2}$. The arrows show the positions where the local 1/2 law can be seen. (*d*) The same as (*a*), now with the Nusselt number scaled with $Ta^{-0.38}$.

turbulent, in both the bulk and boundary layer, and the so-called 'ultimate' regime appears, with an effective scaling law close to $Nu_\omega \sim Ta^{0.38}$ (Ostilla-Mónico *et al.* 2014a,b).

The situation is more complicated for the grooved TC flow. As shown in figure 3, for the case of $\delta = 0.052d$, three different scaling laws are found with increasing *Ta*: at the early stage, the effective scaling follows the same $Nu_\omega \sim Ta^{1/3}$, as long as *Ta* is smaller than a threshold Taylor number Ta_{th}, at which the effective scaling exponent β in the grooved cases starts to deviate from the smooth cases. Once $Ta > Ta_{th}$, Nu_ω for the grooved wall cases increases with a steeper exponent β than for the smooth wall counterpart. The exponent β can locally be 1/2 for this region. However, further increasing *Ta* leads to a saturation to the ultimate regime effective scaling $Nu_\omega \sim$
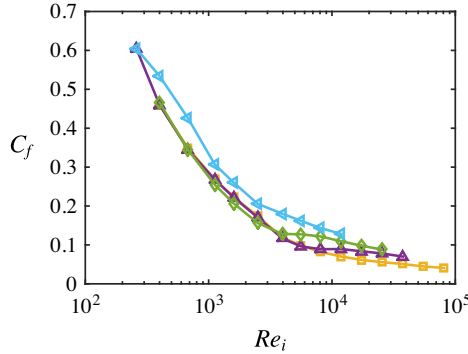
FIGURE 4. (Colour online) Friction factor $C_f = 2\pi Nu_\omega J_0^\omega \nu^{-2}/Re_i^2$ as a function of the inner cylinder Reynolds number Re_i. □, smooth walls simulations by Ostilla-Mónico *et al.* (2014*a*); △, grooved walls simulations with $\delta = 0.052d$; ◇, grooved walls simulations with $\delta = 0.105d$; ◁, grooved walls simulations with $\delta = 0.209d$.

$Ta^{0.38}$, as already seen for smooth walls, but with a larger prefactor. This means that the influence of the grooves on the effective scaling exponent becomes weaker with increasing Ta.

Note that Nu_ω does not always increase after Ta exceeds the threshold Ta_{th}. For the case of $\delta = 0.105d$, at $Ta < Ta_{th}$, the relations between Nu_ω and Ta of smooth and grooved cases still follow the same route. But, after $Ta > Ta_{th}$, there is a region where Nu_ω decreases. The largest decrease is 5 % and occurs at $Ta = 1.0 \times 10^7$. The mechanism will be shown and explained in detail in §4. This can be related to channel flow in which Choi *et al.* (1993) also found drag reduction in a specific range of Re. With a further increase in Ta, when $Ta > 2.5 \times 10^7$, the exponent β starts to increase and can locally be as steep as $1/2$. Again, after that, the effective scaling saturates once Ta is large enough.

For $\delta = 0.209d$, the threshold Ta_{th} is at approximately $Ta = 1.0 \times 10^5$. After a small range of steep regime in which the slope is larger than 0.38, we find only an upward shift of Nu_ω. The effective scaling law does not change much, either in the laminar or in the turbulent region. This suggests that these massive grooves cannot shift the transition to the ultimate regime to even smaller value of Ta.

At given Ta, we find that a larger groove height causes a more profound increase of Nu_ω. For example, after saturation, for the cases of $\delta = 0.052d$, $\delta = 0.105d$ and $\delta = 0.209d$, Nu_ω increases by 41 %, 58 % and 68 %, respectively. The enhanced transport in TC flow with grooved walls therefore cannot be solely ascribed to the surface area increase; it is rather the local flow dynamics near the grooves which enhances the transport. In the following sections we will look into the flow details to explore the mechanism of Nu_ω increase which goes beyond the pure increase of surface area by the grooves. Note that the behaviour of Nu_ω versus Ta can also be expressed in terms of the friction factor

$$C_f = 2\pi Nu_\omega J_0^\omega \nu^{-2}/Re_i^2, \qquad (3.1)$$

as a function of the inner cylinder Reynolds number Re_i, which is shown in figure 4. From this definition, we find that once the local scaling exponent between Nu_ω and Ta equals $1/2$, a plateau can be found in the C_f versus Re_i relation.
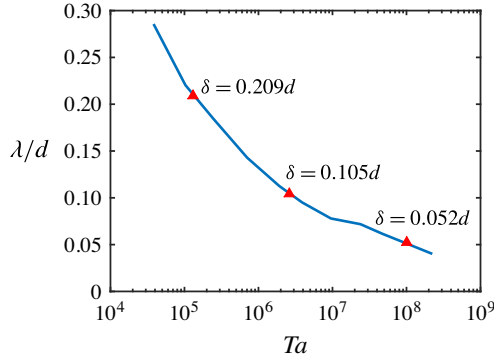
FIGURE 5. (Colour online) Comparison between boundary layer thickness λ and groove height δ. The solid line denotes the averaged boundary layer thickness estimated by $\lambda \simeq d\sigma/(2Nu_\omega)$ (Brauckmann & Eckhardt 2013). Each triangle symbol shows the value of Ta at which the groove height equals the boundary layer thickness.

It is a common finding that, in RB flow, the surface roughness becomes active only when the thermal boundary layer is thinner than a characteristic roughness height (Shen *et al.* 1996; Stringano *et al.* 2006). Similar to this, we also want to stress that, in TC flow with grooves, the effect of grooves on Nu_ω can only be seen when the BL thickness λ becomes less than the groove height δ. At small Ta, the BL is very thick, and thus the grooves are buried under the BL and the fluid cannot feel their influence. At large Ta, the BL becomes thinner than the grooves, and thus they strongly affect the BL dynamics and thereby alter the transport properties. At this critical value Ta_{th}, the BL thickness equals the groove height. The averaged BL thickness λ in TC flow can be estimated by $\lambda \simeq d\sigma/(2Nu_\omega)$ (Brauckmann & Eckhardt 2013), where σ is defined as $\sigma = [(r_i + r_o)/(2\sqrt{r_o r_i})]^4$. Indeed, our simulations show that Nu_ω starts to change once the boundary layer thickness becomes smaller than the groove height. As shown in figure 5, for cases of $\delta = 0.209d$, $\delta = 0.105d$ and $\delta = 0.502d$, we have $Ta_{th} \simeq 1.0 \times 10^5$, $Ta_{th} \simeq 2.8 \times 10^6$ and $Ta_{th} \simeq 9.0 \times 10^7$, respectively. Also from figure 3 it is found that there are sharp transitions for Nu_ω at these points.

We stress that the local exponent $\beta \approx 1/2$ we have found in figure 3 (see the arrows) is not the ultimate region scaling without logarithmic correction, but just a crossover between a regime where the groove depth is less than the BL thickness and a regime where the groove depth is larger than the BL thickness. Hence it is fortuitous to find this 1/2 exponent in TC flow with grooves. Note that in pipe flow (Nikuradse 1933) and TC flow with perpendicular roughness (van den Berg *et al.* 2003) the situation is different. In both cases, the roughness is orthogonal to the flow direction and the main flow is impeded by the roughness. The transfer of momentum from the fluid to the wall is accomplished by the drag on the roughness elements, which at high Re is predominantly by pressure forces, rather than by viscous stresses. A new length scale of the groove height is thus implemented into the system and the drag is independent of Re at high Re (Pope 2002). In contrast, in our current simulations with grooves, these are aligned with the flow direction. As a result, the grooves do not play an immediate role in generating drag, and there is no new length scale to be implemented into the BL. With increasing Ta, the viscous stresses still dominate the drag. Therefore, the exponent β saturates to the same value as for the smooth case at larger Ta. It is important to note that, in RB flow, the large-scale flow fluctuates, and so it always
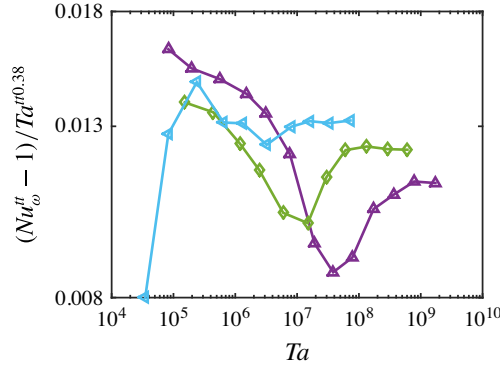
FIGURE 6. (Colour online) Tip-to-tip Nusselt number as a function of the tip-to-tip Taylor number scale with $Ta^{tt-0.38}$ for $\eta = 0.714$. $\triangle$, grooved walls simulations with $\delta = 0.052d$; $\diamondsuit$, grooved walls simulations with $\delta = 0.105d$; $\triangleleft$, grooved walls simulations with $\delta = 0.209d$. Comparing this figure with figure 3(d), we find no change in the scaling exponent.

sees the roughness as small obstacles generating direct drag. This aspect is different from TC flow. However, drag in TC flow is caused by the wall shear rate of the azimuthal velocity. This is analogous to the wall gradient of the temperature in RB flow, not to the drag caused by the velocity field.

From the above findings, we summarize that, compared to smooth cases, in grooved wall TC flow there are three different characteristic regimes. First, when $Ta < Ta_{th}$, smooth and groove cases show the same behaviour. Second, when $Ta > Ta_{th}$, the scaling exponent β increases to be locally as large as $1/2$. Third, when Ta is large enough, there is a saturation regime in which the exponent β saturates back to the ultimate region effective scaling law 0.38, but the prefactor of Nu_ω is increased by a substantial margin.

So far, the Ta and Nu_ω depicted here are both based on the base-to-base distance d. The usage of d follows the convention of RB studies (Du & Tong 2000; Stringano *et al.* 2006). This choice, however, is quite arbitrary, because d is only one possibility for the reference length. The tip-to-tip distance could also be selected to non-dimensionalize Ta and Nu_ω. Such a definition would then lead to the tip-to-tip Taylor number $Ta^{tt} = Ta(d - 2\delta)^2/d^2$ and Nusselt number $Nu_\omega^{tt} = Nu_\omega(d - 2\delta)r_i^2 r_o^2/[d(r_i + \delta)^2(r_o - \delta)^2]$. In figure 6, we show Nu_ω^{tt} as a function of Ta^{tt}. Despite the grooves being quite high in our simulations, different choices of the characteristic length scale do not affect the effective power laws, but only the exact values of the transitional Ta numbers. Therefore, it is a reasonable choice that we only use d as the reference length scale. If the system reached the ultimate state, one would expect that the transport of torque should be the same, i.e. the Nu_ω versus Ta relation should be the same as that for the smooth case. When deducing the surface area increase, in our current simulations of $\delta = 0.052d$, $\delta = 0.105d$ and $\delta = 0.209d$, Nu_ω increases by -1%, 12% and 18% compared to the smooth case, respectively. We expect that these differences become smaller and smaller with increasing Ta. Simulations with higher Ta are required to resolve this question.

4. Flow structures

In order to find the mechanism behind the Nu_ω increase, in this section, visualizations of the flow in the bulk and the grooves are shown to compare the grooved and smooth
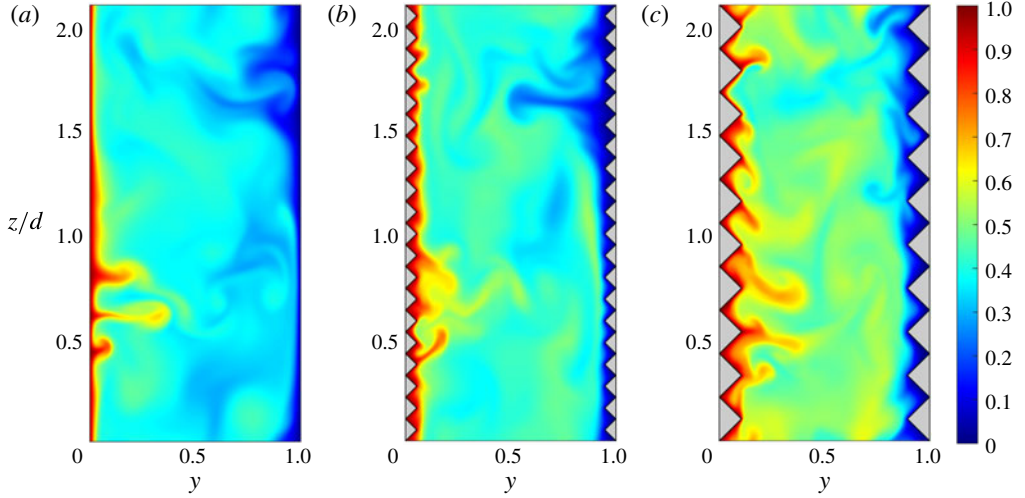
FIGURE 7. (Colour online) Contour plots of the instantaneous azimuthal velocity field u_θ for (*a*) the smooth, (*b*) the $\delta = 0.052d$, and (*c*) the $\delta = 0.105d$ cases at $Ta = 4.77 \times 10^7$. The colour scale goes from azimuthal velocity 0 (blue) to 1 (red). In the smooth case, the flow is in the transition region where the laminar regions in the boundary layer coexist with turbulent, plume-ejecting areas. In (*b*), the boundary layer is still thicker than the groove, and therefore no evident difference can be distinguished between (*a*) and (*b*). For (*c*), the boundary layer is thinner than the grooves and plumes are ejected from all tips of the grooves.

cases. Figure 7 shows three contour plots of the instantaneous azimuthal velocity u_θ in the meridional plane for the smooth and the $\delta = 0.052d$ and $\delta = 0.105d$ cases at $Ta = 4.77 \times 10^7$. Figure 7(*a*) shows the flow in the transition region where the laminar zones in the BL coexist with turbulent, plume-ejecting areas. These plumes are associated with the axial and radial structure which is induced by the Taylor vortices. Plumes are ejected from preferential positions where there are adverse pressure gradients such that detachment from the BL is supported. In figure 7(*b*), where $\delta = 0.052d$, Ta is still smaller than Ta_{th}, which also means that the grooves are still buried within the BL and hence the effect of the grooves is very small. This is the reason why obvious differences cannot be distinguished between figure 7(*a*) and (*b*). However, for figure 7(*c*), where $\delta = 0.105d$, $Ta > Ta_{th}$ and the power law between Nu_ω and Ta, which can be seen from figure 3, is in the steep regime. We find that plumes are ejected from all the tips of the grooves. It is interesting to note that, for the smooth case, the plumes are ejected only from some specific regions, while for the grooved case, plumes are detached from nearly all the tips of the grooves. Because more plumes are ejected compared to the smooth case, Nu_ω is greatly enhanced, and the larger exponent β regime can be seen in figure 3.

Figure 8 shows three contour plots of the instantaneous azimuthal velocity u_θ in the meridional plane for the smooth, and the $\delta = 0.052d$ and $\delta = 0.105d$ cases at $Ta = 9.75 \times 10^8$. Figure 8(*a*) shows the flow in the fully turbulent region. Due to the decrease in the wall pressure gradient in the axial direction, plumes are ejected from more places compared to $Ta = 4.77 \times 10^7$. For figure 8(*b*), where $\delta = 0.052d$, we have $Ta > Ta_{th}$, and thus we can see that more plumes are ejected due to the existence of grooves. The groove tips are the preferential places for these ejections.
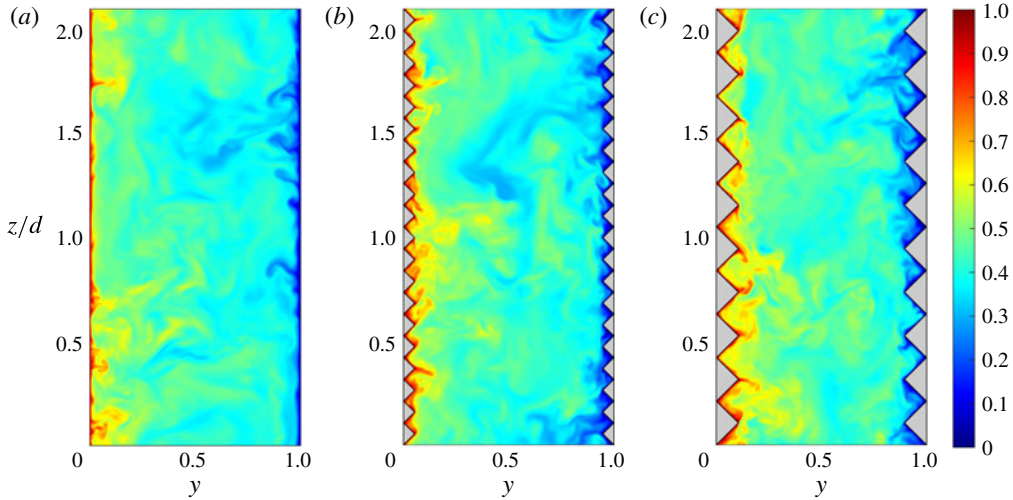
FIGURE 8. (Colour online) Contour plots of the instantaneous azimuthal velocity field u_θ for (a) the smooth, (b) the $\delta = 0.052d$, and (c) the $\delta = 0.105d$ cases at $Ta = 9.75 \times 10^8$. The colour scale goes from azimuthal velocity 0 (blue) to 1 (red). In the smooth case, the flow is in the fully turbulent region where the bulk and boundary both become turbulent. Due to the decrease of wall pressure gradient in the axial direction, plumes are ejected from more places compared to $Ta = 4.77 \times 10^7$. In (b) and (c), where $Ta > Ta_{th}$, plumes are ejected from the tips, and these plumes all show preferential directions which follow the Taylor vortices.

In figure 8(c), for the case of $\delta = 0.105d$, compared to the smooth case, plumes are still ejected from the tips of grooves, but near the valleys there are spots where plumes grow. The difference in the number of plumes between the grooved and smooth cases reduces with increasing Ta. This maybe another reason why the Nu_ω versus Ta scaling saturates at high Ta. In addition, we note that these plumes have different directions of movement, either to the top or bottom. It is interesting to find that these plumes follow the direction of Taylor vortices, which also means that Taylor vortices still exist even if there are grooves. This behaviour can be explained by the association between the large-scale Taylor vortices and the secondary vortices inside the grooves, which we will show in the following paragraphs.

One may argue that plumes may only be emitted at some points of the groove tips. This, however, is not the case. Figure 9 shows contour plots of the instantaneous azimuthal velocity u_θ of the smooth and $\delta = 0.105d$ cases for Taylor number $Ta = 9.75 \times 10^8$ at constant radius cuts. In figure 9(a), at wall distance $y = (r - r_i)/d = 4 \times 10^{-3}$, the flow is in the BL and herring-bone streaks can be seen due to the boundary layer instability. While, in figure 9(b), at wall distance $y = (r - r_i)/d = 0.106$ or wall distance in terms of the tip of grooves $y' = (r - r_i - \delta)/d = 1 \times 10^{-3}$, the flow is very close to the tips of the grooves, high-speed plumes (shown in red) can be identified almost everywhere near the tips of the grooves. It is also seen from this panel that evidence of large-scale vortices can be identified between high-speed regions where there are large zones of low speed. This is because in these regions flows are driven by Taylor rolls and move from the outer to the inner cylinder or vice versa. In addition, the flow is statistically homogeneous in the θ direction. Both panels can serve as a confirmation of this assumption.
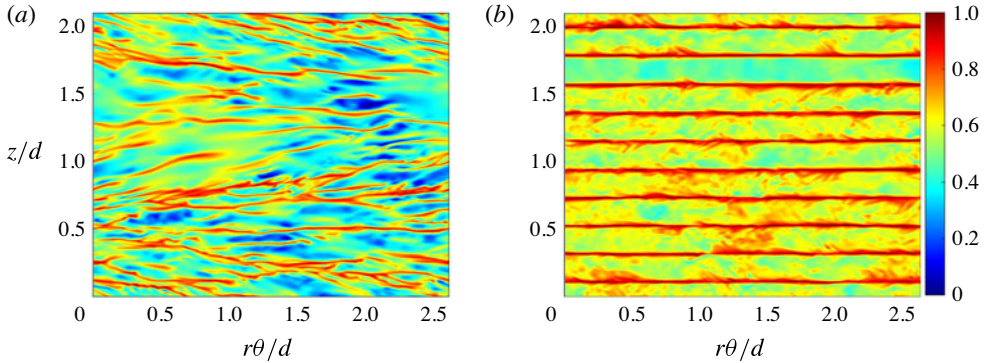
FIGURE 9. (Colour online) Contour plots of the instantaneous azimuthal velocity $u_\theta(\theta, z)$ for Taylor number $Ta = 9.75 \times 10^8$ at constant radius cuts. The colour scale goes from azimuthal velocity 0 (blue) to 1 (red). (*a*) The smooth case at fixed wall distance $y = (r - r_i)/d = 4 \times 10^{-3}$. (*b*) The $\delta = 0.105d$ case at fixed wall distance in terms of the tip of grooves $y' = (r - r_i - \delta)/d = 1 \times 10^{-3}$. (*a*) Shows the herring-bone streaks in the boundary layer while (*b*) shows plumes being ejected homogeneously along the azimuthal direction.
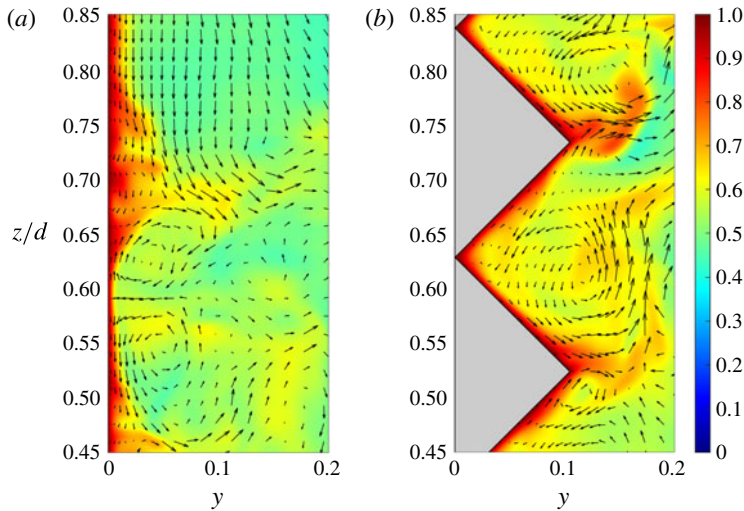
FIGURE 10. (Colour online) Enlargement of the near-wall region for contour plots of the instantaneous azimuthal velocity u_θ superposed with instantaneous velocity vectors in the meridional plane at $Ta = 9.75 \times 10^8$. (*a*) The smooth case, (*b*) the $\delta = 0.105d$ case. The colour scale goes from azimuthal velocity 0 (blue) to 1 (red). The velocity vectors are formed by the axial and radial velocity on the surface. For the smooth case in (*a*), the plumes are induced by the acceleration of radial flow. Then vortex rings are formed. For the grooved configuration in (*b*), the axial flow drives the secondary vortex inside the grooves. At the same time the interaction between the secondary vortex and the Taylor rolls causes the detachment of the boundary layer from the tips of the grooves. The detached azimuthal flow then develops into a plume.

We now discuss why plumes are preferentially ejected from the tips of the grooves. Figure 10 shows the contour plots of the instantaneous azimuthal velocity u_θ,
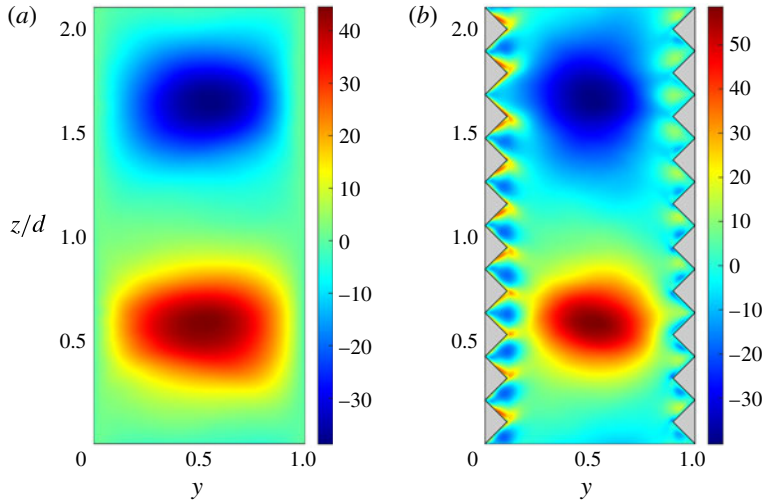
FIGURE 11. (Colour online) Contour plots of the time- and azimuthally averaged correlation $r^3 \langle u_r \omega \rangle_{A,t}$ at $Ta = 9.75 \times 10^8$. (a) The smooth case, (b) the $\delta = 0.105d$ case. The correlation has been normalized according to $r^3 \langle u_r \omega \rangle_{A,t} / (J_0^\omega Nu_\omega)$. The red colour represents the largest value while the blue colour represents the smallest value. It can be seen from the comparison that the interaction between the secondary vortices inside the grooves and large-scale Taylor rolls enhances the convective part of the transport in the near-tip regions.

which are enlargements of the plume-detaching region of figure 8, superposed by instantaneous velocity vectors in the meridional plane. Figure 8(a) shows how plumes detach from the wall of the inner cylinder. A radial pressure gradient accelerates the fluid in the central part of the plume. The sudden acceleration generates secondary vorticity close to the plume, deforming the plume into a mushroom shape. However, for the grooved case, the situation is completely different. The axial pressure gradient favours the Taylor vortex propelling a secondary vortex inside the grooves. This secondary vortex has the opposite direction compared to the large-scale Taylor vortex. The interaction between the Taylor vortex and the secondary vortex causes the detachment of the BL from the tips of the grooves into the bulk, and hence forms a plume. Then the plumes are dissipated into the large-scale Taylor rolls. These phenomena are clearly seen in figure 8(b). We note that it is very similar to the famous 'lid-driven-cavity' flow – however, it is the Taylor roll that drives the flow in the grooves. Although in RB flows the mechanism for large-scale rolls is different from TC flow, similar thermal plumes are also found to be ejected from the tips of roughness elements there (Du & Tong 2000; Stringano *et al.* 2006).

It can be seen from figure 10 how plumes enhance Nu_ω as well. From the definition of angular velocity current J_ω (equation (2.1)), it is known that Nu_ω consists of two parts: convective and conductive contributions. The convective contribution is proportional to the correlation $r^3 \langle u_r \omega \rangle_{A,t}$. The interaction between the secondary vortex inside the grooves and the Taylor vortex first induces a radial velocity at the tips, then lifts the BL. The geometrically induced radial flow separation, together with the BL detachment, greatly enhances the convective part of the Nusselt number. As evidence of this, in figure 11, a comparison of the correlation $r^3 \langle u_r \omega \rangle_{A,t}$ at the same $Ta = 9.75 \times 10^8$ between the smooth and $\delta = 0.105d$ cases is performed. From
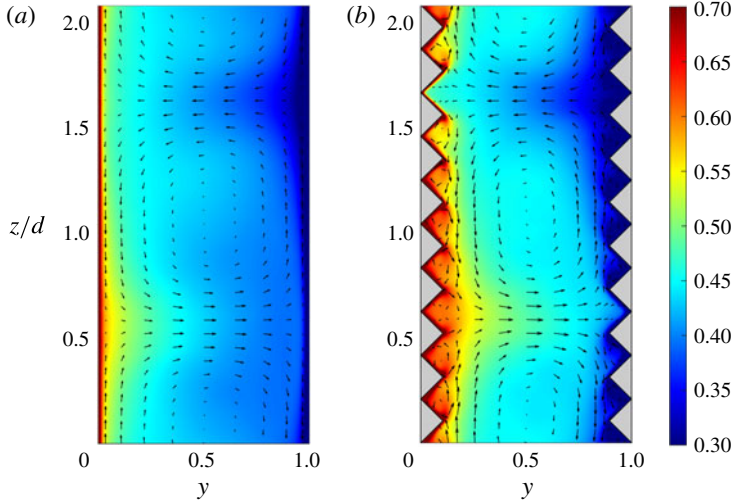
FIGURE 12. (Colour online) Contour plots of the time- and azimuthally averaged azimuthal velocity $\langle u_\theta \rangle_{\theta,t}$ superposed by time- and azimuthally averaged velocity vectors in the meridional plane at $Ta = 9.75 \times 10^8$. (*a*) The smooth case, (*b*) the $\delta = 0.105d$ case. The colour scale goes from azimuthal velocity 0.3 (blue) to 0.7 (red). It can be seen from the comparison that the interaction between the secondary vortices inside the grooves and large-scale Taylor rolls favours the circulation of Taylor rolls, and hence we get enhanced transport.

figure 11(*b*), it is seen that the BL is thin enough for the grooves to protrude from it, so that, in this case, the interaction of the secondary vortex inside the grooves with the Taylor rolls contributes to the total angular momentum transport, while the additional activity in the near-tip region determines the extra transport increase. In other words, the grooves enhance plume generation and allow the plumes to be ejected towards the Taylor rolls. The combined mechanisms then increase the convective part of torque transport.

From another point of view, we have mentioned before that large-scale Taylor vortices still exist in grooved TC flow. In figure 12, time-averaged azimuthal velocity contour plots with superposed velocity vectors are presented for the smooth and the $\delta = 0.105d$ configurations at $Ta = 9.75 \times 10^8$. Figure 12(*a*) corresponds to a flow field in the ultimate regime. The Taylor roll is still present, but weaker, and plumes are ejected from many places on the surface. As a comparison, in figure 12(*b*) it is seen that the large-scale Taylor roll interacts with the secondary vortex inside the grooves, and therefore we conclude that, because of these grooves, on one hand, the Taylor roll induces recirculation inside the grooves, and at the same time the secondary vortex also favours the flow of Taylor rolls more effectively than the smooth case. We define a wind Reynolds number as $Re_w = \sigma(u_r)d/\nu$, where $\sigma(u_r)$ is the standard deviation of the radial velocity. For this figure, we find $Re_w(\text{grooved}) = 1.12Re_w(\text{smooth})$. In this case the presence of grooves generally leads to a stronger Taylor roll, which also contributes to the convective part of torque transport.

If, in contrast, the fluctuation of the Taylor roll is not strong enough to induce the secondary vortex inside the grooves, then stagnant flow inside the grooves could not favour the Taylor vortices. Oppositely, the grooves impede the circulation of Taylor rolls when the rolls flow past the grooves. In figure 13, a time-averaged azimuthal
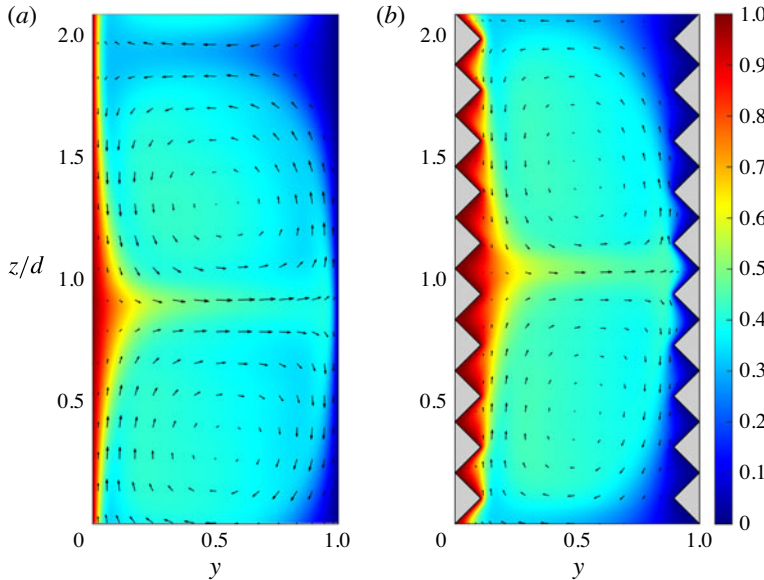
FIGURE 13. (Colour online) Contour plots of the time- and azimuthally averaged azimuthal velocity $\langle u_\theta \rangle_{\theta,t}$ superposed by time- and azimuthally averaged velocity vectors in the meridional plane at $Ta = 9.52 \times 10^6$. (a) The smooth case, (b) the $\delta = 0.105d$ case. The colour scale goes from azimuthal velocity 0 (blue) to 1 (red). Comparing the two panels, no evident secondary vortices can be identified inside the grooves, which serve only as obstacles to the Taylor rolls. This is the reason why in some cases we find that Nu_ω is decreased.

velocity contour plot with superposed velocity vectors is presented for the $\delta = 0.105d$ configuration at $Ta = 9.52 \times 10^6$. No evident secondary vortices can be seen inside the grooves. Also, no large separation of Taylor rolls can be identified and these grooves serve only as obstacles to hinder the flow from crossing them. For this figure, we find $Re_w(\text{grooved}) = 0.84Re_w(\text{smooth})$. As a result, weaker Taylor vortices reduce the radial angular velocity transport, and Nu_ω is decreased.

In the above paragraphs, we discussed how grooves affect the bulk flow and the convective part of Nu_ω. Because of the conservation of angular velocity current J^ω along the radius, the grooves will also have an impact on the wall turbulence structure and wall shear rate. To further illustrate the mechanism increasing or decreasing Nu_ω, here we include a snapshot of the instantaneous streamwise (azimuthal) vorticity field, as shown in figure 14 for $Ta = 9.52 \times 10^6$ and $Ta = 9.75 \times 10^8$ with $\delta = 0.105d$. This figure shows the streamwise vorticity field superposed by the velocity vectors in the plane. At $Ta = 9.52 \times 10^6$, there is almost no secondary vortex between the grooves, and only at the tips of the grooves do we see the streamwise vortices which are caused by flow separation there. At $Ta = 9.75 \times 10^8$, the secondary vortex is much stronger compared to that of the $Ta = 9.52 \times 10^6$ case. Between groove tips, almost all surface areas of grooves are exposed to the sweep motion that streamwise vorticity (secondary vortex) induces. The stronger the secondary vortex, the greater the surface area exposed to the sweep motion it induces, and hence the higher the shear rate of azimuthal velocity. We refer later, in figures 21 and 22, to how secondary vortices gradually occupy the entire region between grooves, and hence increase the shear rate not only at the tips, but also in the valleys, with increasing Re.
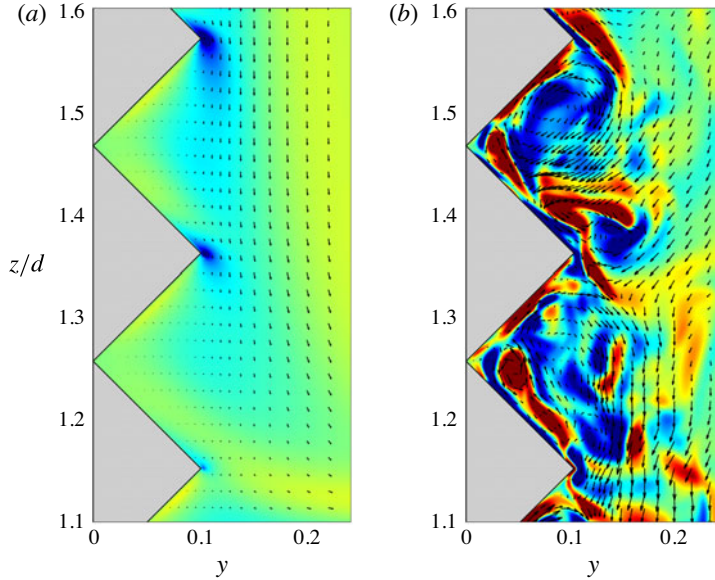
FIGURE 14. (Colour online) Enlargement of the near-wall region for contour plots of the instantaneous streamwise vorticity field superposed with instantaneous velocity vectors in the meridional plane at $Ta = 9.52 \times 10^6$ (*a*) and $Ta = 9.75 \times 10^8$ (*b*) with $\delta = 0.105d$. The black arrows show the velocity vectors in the plane. Blue denotes a negative streamwise vorticity and red a positive streamwise vorticity.
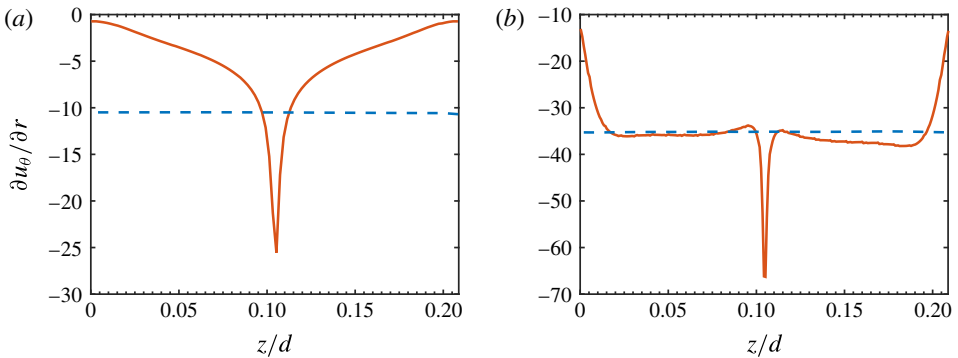

FIGURE 15. (Colour online) Wall shear rate $\partial u_\theta / \partial r$ averaged in time, azimuthally, and over ten grooves for the $\delta = 0.105d$ case at two different Taylor numbers: (*a*) $Ta = 9.52 \times 10^6$; (*b*) $Ta = 9.75 \times 10^8$. The solid lines denote the grooved case and the dashed line the averaged wall shear rate for the smooth case at the same Ta.

We now turn to discussing how the secondary vortices are related to the wall shear rate of the azimuthal velocity, and hence Nu_ω. In figure 15, we show the azimuthal shear rate averaged in time, azimuthally, and over ten grooves at two different Taylor numbers $Ta = 9.52 \times 10^6$ and $Ta = 9.75 \times 10^8$, compared with the results in the smooth case. At $Ta = 9.52 \times 10^6$, without secondary vortices, only the tips of the grooves are exposed to the shear of the Taylor rolls, and the shear rate decays very quickly to zero from the tips to the valleys of the grooves. There is just a small region close
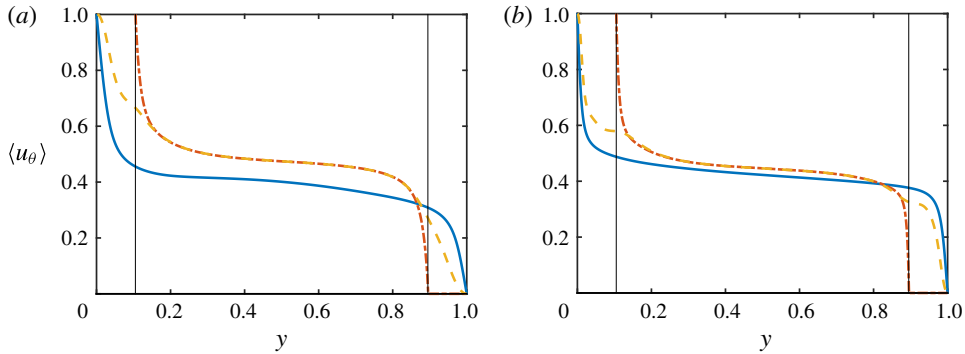
FIGURE 16. (Colour online) Averaged azimuthal velocity profile along a radius for the smooth and the $\delta = 0.105d$ case at two different Taylor numbers: (*a*) $Ta = 4.77 \times 10^7$; (*b*) $Ta = 9.75 \times 10^8$. The solid line shows the time-, azimuthally and axially averaged velocity profile for the smooth case. The dashed line denotes the grooved case profile over time, azimuth and ten valleys, while the dot-dashed line denotes time, azimuth and ten tips, respectively.

to the groove tip where the shear rate is larger than that in the smooth case. That is why the torque is reduced. However, at $Ta = 9.75 \times 10^8$, with strong secondary vortices, the strong mixing effect causes almost the entire surface area to be exposed equally to the high shear rate. Only very close to the valley, can one find that the shear rate is smaller than its smooth counterpart. That is why the torque is enhanced. The mechanism proposed here is similar to that in channel flow with riblets, where the location of quasistreamwise vortices is changed by the size of the grooves, and thus turbulence drag increases or decreases according to the groove size (Choi *et al.* 1993). However, we observe only very few cases at one groove height $0.1d$ with Ta number of approximately 10^7 where torque is reduced. At this Ta, the flow is not fully turbulent, and we would restrict our analysis to specific cases. Indeed, more work is needed to explore whether drag reduction is possible for fully turbulent TC flow.

5. Boundary layer dynamics

In this section we focus on the question of how exactly the grooves modify the BL dynamics. Figure 16 shows the mean velocity profiles in the smooth and in the $\delta = 0.105d$ configuration at $Ta = 4.77 \times 10^7$ and at $Ta = 9.75 \times 10^8$. At the smaller Ta the scaling slope is larger than the effective ultimate regime scaling 0.38, while at the larger Ta the effective scaling saturates back to 0.38. By choosing these two Ta, we can thus directly compare the BL differences between these two regimes. It is seen from this figure that the bulk velocity increases in the presence of wall roughness, i.e. the influence of the wall roughness penetrates well into the bulk region of the flow, because of the conservation of the angular velocity current $J^\omega = r^3(\langle u_r \omega \rangle_{A,t} - \nu \partial_r \langle \omega \rangle_{A,t})$ along the radius. Figure 17 shows an enlarged region of figure 16 near the wall of the inner cylinder. The velocity profile for the smooth case is time-, azimuthally, and axially averaged, while for the grooved case it is time- and azimuthally averaged for ten different tip points and valley points of the grooves. For the smooth case, the velocity profile indicates that, due to turbulent mixing induced by the Taylor rolls, the azimuthal velocity is uniform in the bulk region and the velocity gradient across the radius is concentrated in thin boundary layers. With increasing Ta, the BL becomes
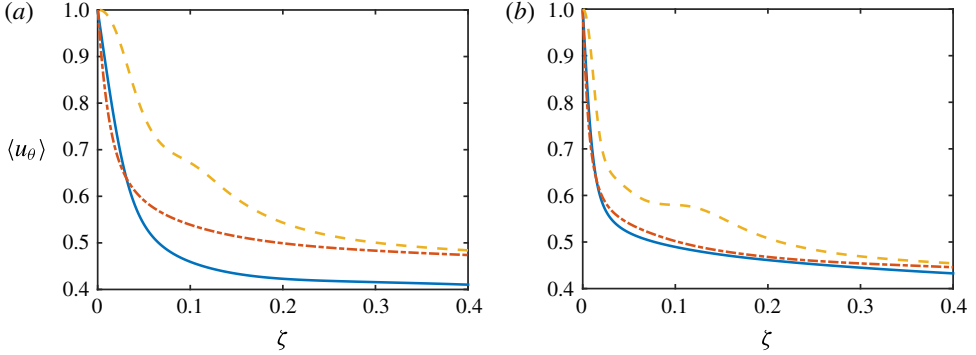
FIGURE 17. (Colour online) A close look at the near inner cylinder region for the averaged azimuthal velocity profile of the smooth and the $\delta = 0.105d$ case at two different Taylor numbers: (a) $Ta = 4.77 \times 10^7$; (b) $Ta = 9.75 \times 10^8$. The solid line shows the time-, azimuthally and axially averaged velocity profile for the smooth case. The dashed line denotes the grooved case profile over time, azimuth and ten valleys, while the dot-dashed line denotes time, azimuth and ten tips, respectively. Note that $\zeta = y - \delta/d$ is the horizontal distance from the solid surface.

thinner and the velocity gradient becomes steeper, as expected. Correspondingly, the azimuthal velocity profile in the bulk becomes flatter and the bulk is more extended towards the walls.

Similar features also apply to TC flow with grooves, but at the same time it also shows some interesting characteristic differences. For the grooved case at $Ta = 4.77 \times 10^7$, the velocity gradient is larger at the tip of the groove, while it attains the minimum value at the valley. This is because the flow trapped inside the groove is viscosity dominated and the secondary vortex is very weak. In comparison, at $Ta = 9.75 \times 10^8$, the secondary vortex inside the groove is strengthened significantly. The strong secondary vortex fully mixes the flow inside the grooves, and even a flat small bulk region can be seen. At the same time, the BL thickness at the valley is greatly decreased as a result of the extension of the secondary vortex. Because the secondary vortex must flow smoothly over the valley, where it is singular, the BL is thicker in the valley as compared to at the tip. We expect the difference of the BL thickness between the tip and valley point to become smaller and smaller on increasing the Ta. The asymmetry of the BL at the inner and outer surfaces is caused by the curvature of the cylinders, and also depends on the strength of the Taylor rolls, as has been detailed in Ostilla-Mónico *et al.* (2014*b*).

The distinctive feature for the ultimate regime is the turbulent BL. For wall distances much larger than the internal length scale and much smaller than the outer length scale, the mean velocity profile has a logarithmic dependence on the distance to the wall. It has been shown in many canonical flows, such as pipe, channel and BL flow, that logarithmic velocity profiles exist. We refer the reader to the reviews by Marusic *et al.* (2010) and Smits, McKeon & Marusic (2011) for a detailed introduction. Figure 18 presents the non-dimensionalized azimuthal velocity $u^+ = (U - \langle u_\theta \rangle_{t,\theta})/u_*$ on tips and valleys as a function of the wall distance y^+ for the inner cylinder boundary layer at $Ta = 9.75 \times 10^8$ for the grooved case. We define u_*, the local friction velocity, as $u_* = (\nu \langle \partial_r u_\theta(r_i) \rangle_{t,\theta})^{1/2}$ for valleys and tips, with ∂_r the derivative normal to the wall and y^+ the non-dimensional wall distance, given by
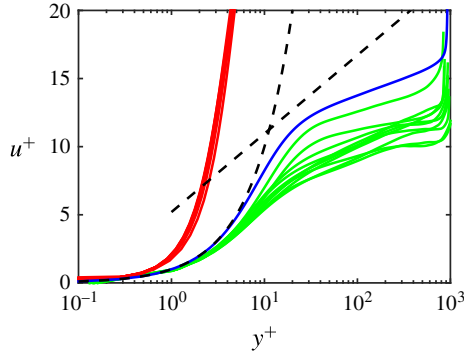
FIGURE 18. (Colour online) Velocity profiles of the smooth and the $\delta = 0.105d$ case non-dimensionalized by friction velocity and wall distance at $Ta = 9.75 \times 10^8$. The ten red and ten green lines represent the non-dimensionalized azimuthal velocity $u^+ = (U - \langle u_\theta \rangle_{\theta,t})/u_*$ over ten valleys and ten tips for the grooved case, which show different interactions with the Taylor rolls. The local friction velocity is defined as $u_* = (\nu \langle \partial_r u_\theta(r_i) \rangle_{t,\theta})^{1/2}$, with ∂_r the derivative normal to the wall, where y^+ is the non-dimensional wall distance $y^+ = (r - r_i)u_*/\nu$ for valleys and $y^+ = (r - r_i - \delta)u_*/\nu$ for tips in wall units. The blue line shows the averaged mean velocity profile for the smooth case at the same Ta. In the smooth case, we also average over the axial direction. That is, replacing $\langle \cdots \rangle_{\theta,t}$ by $\langle \cdots \rangle_{\theta,t,z}$ in the above definitions, with the wall distance being the same as the one used for the valleys. The dashed lines show the relationships $u^+ = y^+$ and $u^+ = 2.5 \ln(y^+) + 5.2$.

$y^+ = (r - r_i)u_*/\nu$ for valleys and $y^+ = (r - r_i - \delta)u_*/\nu$ for tips in terms of wall units. As a comparison, in figure 18 we also plot the averaged mean velocity profile for the smooth case at the same Ta. That is, by replacing $\langle \cdots \rangle_{t,\theta}$ with $\langle \cdots \rangle_{t,\theta,z}$ in the above definitions, with the wall distance the same as the one used for valleys. In the smooth case, the mean velocity profile is first linear in the viscous region, then after a buffer region becomes logarithmic. For the grooved case, significant downward shifts in the log-law are obtained near the tips, whereas significant upward shifts are obtained near the valleys. Because of the strong plume ejection, all tips of grooves show logarithmic behaviour in the boundary layer, in accordance with the findings by Ostilla-Mónico *et al.* (2014*a*) and van der Poel *et al.* (2015*b*), which show that the BL is turbulent at the place where plumes are ejected. The implication is that a specific layout of grooves with tips could locally induce turbulent BLs at specific points. Meanwhile, because Taylor rolls still exist, the plumes have to follow the direction of the Taylor rolls, which results in the different velocity profile slopes for the logarithmic region at different tips (also see figure 12*b*). In the valley, as described before, the BL is thicker than at the tip, so that the flow is more viscosity dominated. It is interesting to note that the velocity profiles nearly overlap in the valleys. This indicates that different secondary vortices at different heights are homogeneous.

The grooves not only influence the mean velocity, but also the fluctuations. Figure 19 shows the root mean square (r.m.s.) azimuthal velocity profiles in the smooth and the $\delta = 0.105d$ configuration at $Ta = 4.77 \times 10^7$ and at $Ta = 9.75 \times 10^8$. Figure 20 shows an enlarged region of figure 19 near the wall of the inner cylinder. The r.m.s. velocity for the smooth case is defined as $(u_\theta)_{rms} = (\langle u_\theta^2 \rangle_{t,\theta,z} - \langle u_\theta \rangle_{t,\theta,z}^2)^{1/2}$, while for the grooved case it is defined as $(\langle u_\theta^2 \rangle_{t,\theta} - \langle u_\theta \rangle_{t,\theta}^2)^{1/2}$, averaged over different tips or valleys. For the smooth case, there is only one peak of the r.m.s. velocity, which is associated with the enhanced fluctuation in the buffer layer. With increasing
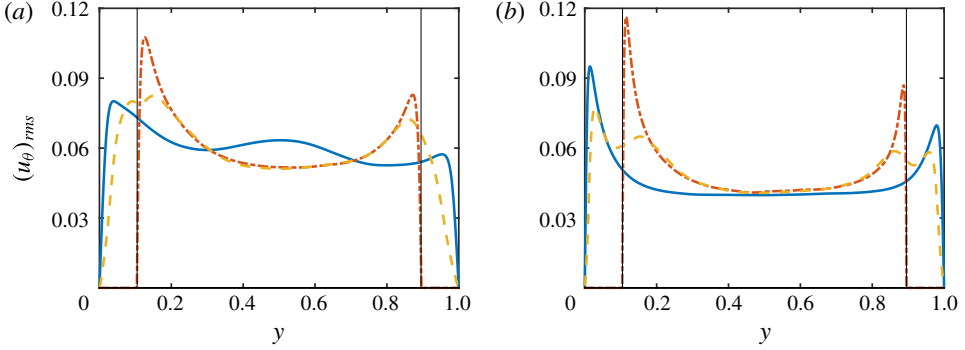
FIGURE 19. (Colour online) Root mean square azimuthal velocity profile of the smooth and the $\delta = 0.105d$ case at two different Taylor numbers: (*a*) $Ta = 4.77 \times 10^7$; (*b*) $Ta = 9.75 \times 10^8$. The solid line shows the time-, azimuthally and axially averaged velocity profile for the smooth case. The dashed line denotes the grooved case profile for valleys, while the dot-dashed denotes the profile above tips. The r.m.s. velocity for the smooth case is defined as $(u_\theta)_{rms} = (\langle u_\theta^2 \rangle_{t,\theta,z} - \langle u_\theta \rangle_{t,\theta,z}^2)^{1/2}$, while for grooved case it is defined as $(\langle u_\theta^2 \rangle_{t,\theta} - \langle u_\theta \rangle_{t,\theta}^2)^{1/2}$ and then averaged over ten different tips or valleys.
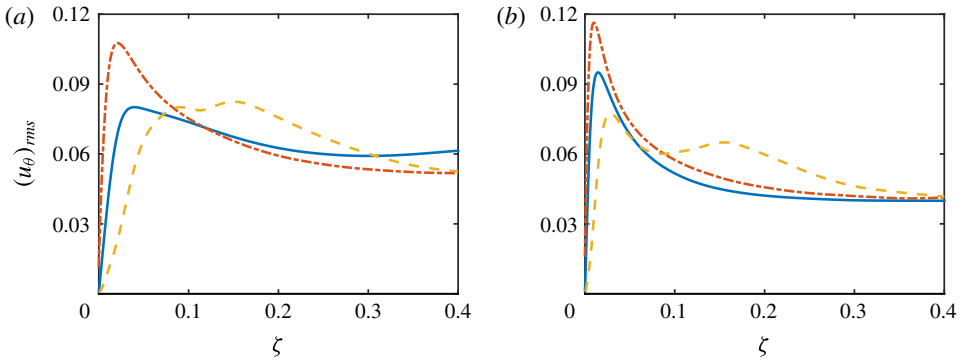

FIGURE 20. (Colour online) A close look at the root mean square azimuthal velocity profile of the smooth and the $\delta = 0.105d$ case in the near-wall region at two different Taylor numbers: (*a*) $Ta = 4.77 \times 10^7$; (*b*) $Ta = 9.75 \times 10^8$. The solid line shows the time-, azimuthally and axially averaged velocity profiles for the smooth case. The dashed line denotes the grooved case profile for valleys, while the dot-dashed denotes the profile above the tips. The r.m.s. velocity for the smooth case is defined as $(u_\theta)_{rms} = (\langle u_\theta^2 \rangle_{t,\theta,z} - \langle u_\theta \rangle_{t,\theta,z}^2)^{1/2}$, while for grooved case it is defined as $(\langle u_\theta^2 \rangle_{t,\theta} - \langle u_\theta \rangle_{t,\theta}^2)^{1/2}$ and then averaged over ten different tips or valleys. Note that $\zeta = y - \delta/d$ is the horizontal distance from the solid surface.

Ta, as the turbulent intensity becomes larger and the BL becomes thinner, and, as expected, the peak is shifted to the inner cylinder and the r.m.s. is larger.

For the grooved case with $Ta = 4.77 \times 10^7$, at the tips of the grooves, the position where the peak occurs is also shifted to the inner cylinder and the r.m.s. velocity is larger. In the valley, we see two different peaks of the r.m.s. velocity. One close to the wall and one close to the bulk. The near-wall peak is associated with the buffer layer and the other peak is associated with the shear layer between the secondary vortex and
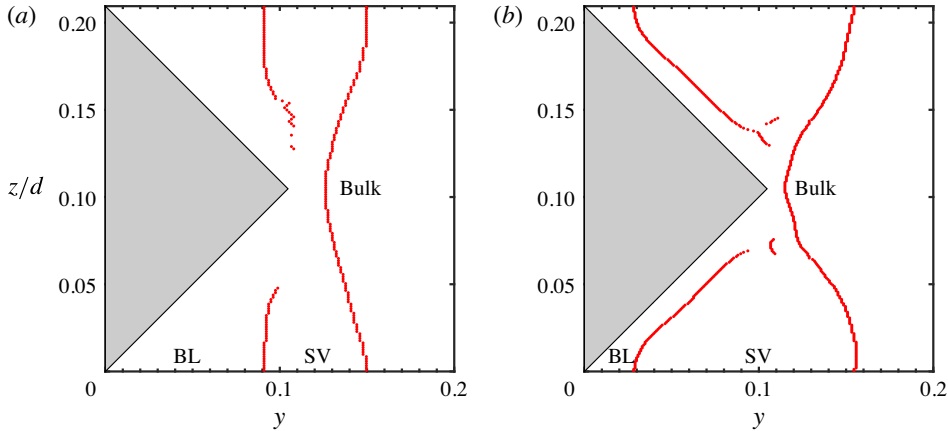
FIGURE 21. (Colour online) The positions of the peaks of the r.m.s. azimuthal velocity profile near the inner cylinder for the $\delta = 0.105d$ cases averaged in time, azimuth and over ten grooves at two different Taylor numbers: (*a*) $Ta = 4.77 \times 10^7$; (*b*) $Ta = 9.75 \times 10^8$. The red points are the positions of these peaks. We average over ten grooves. Abbreviations: BL = boundary layer, SV = secondary vortex.

the Taylor roll. The secondary vortex is located between these two peaks. Because the flow inside the groove is viscosity dominated and laminar, the position of this peak is far away from the wall and the intensity is less than in the shear layer. At $Ta = 9.75 \times 10^8$, the secondary vortex becomes stronger and extends closer towards the wall, as illustrated before. As a result, the BL becomes thinner and shifts closer to the wall; at the same time, the intensity of fluctuation becomes higher than the shear layer.

Figure 21 shows the positions where the peaks of the r.m.s. azimuthal velocity profiles close to the inner cylinder occur for $Ta = 4.77 \times 10^7$ and for $Ta = 9.75 \times 10^8$, both for the $\delta = 0.105d$ case. The profiles were averaged in the azimuthal direction, in time and over the ten grooves. Although other definitions are possible, inspired by the work of Stringano *et al.* (2006), we define the near-wall peak of the r.m.s. velocity profile as the thickness of the boundary layer. This enables us to separate the flow domain into three zones. Between the wall and the near-wall peak is the BL layer zone. Between the two peaks is the secondary vortex zone, and beyond is the bulk zone. From the comparison between these two panels, it is seen that, with increasing *Ta*, the BL inside the groove becomes thinner and more uniformly distributed along the surface of the groove. This indicates that, at high *Ta*, the azimuthal velocity can not feel the effect of the grooves, and thus forms the uniformly thick BL, just as in the smooth case. As an indication of the growing strength of the secondary vortices, in figure 22 we show the distance between the peaks of the r.m.s. azimuthal velocity in the groove valley as a function of *Ta* for the $\delta = 0.105d$ case. It is found that the size of the secondary vortex saturates to $0.11d$.

Finally, to shed further light on why the effective scaling is larger than 0.38 at $Ta = 4.77 \times 10^7$ and saturates back to 0.38 at $Ta = 9.75 \times 10^8$ for the $\delta = 0.105d$ series, we compare the energy dissipation rate $\epsilon_u = \nu \langle (\nabla \boldsymbol{u})^2 \rangle_{t,\theta,z}$ along the radius, as shown in figure 23. According to Grossmann & Lohse (2011), the logarithmic correction, which originates from the turbulent boundary layer, leads to an effective scaling of 0.38. Even in the fully turbulent regime in which we are, the boundary layer effects
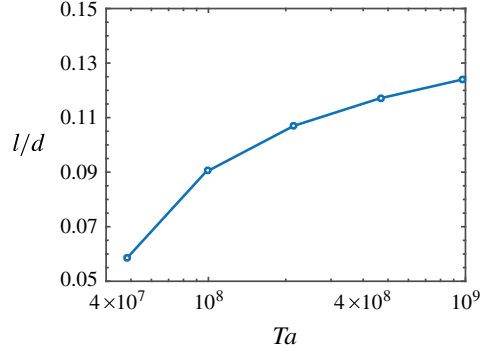
FIGURE 22. (Colour online) Distance l/d between the peaks of the root mean square azimuthal velocity in the groove valley as a function of Ta for the $\delta = 0.105d$ cases.
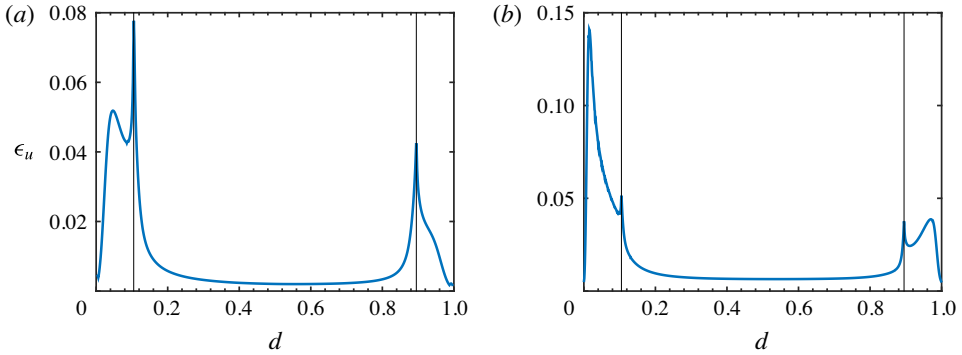

FIGURE 23. (Colour online) Energy dissipation rate $\epsilon_u = \nu \langle (\nabla \boldsymbol{u})^2 \rangle_{t,\theta,z}$ along the radius for the $\delta = 0.105d$ series. It was averaged in time, azimuth and height at two different Ta: (a) $Ta = 4.77 \times 10^7$; (b) $Ta = 9.75 \times 10^8$.

still play a major role in determining the scaling exponent. Only asymptotically, will the Nu versus Ta scaling exponent go to $1/2$, but we are far away from this exponent in any experiment. At $Ta = 9.75 \times 10^8$, because the BL inside the groove becomes more similar to the smooth case, the contribution of the BL to the energy dissipation returns. As a result, the logarithmic correction to the scaling law occurs. At $Ta = 4.77 \times 10^7$, the BL inside the groove is thick and laminar; however, this is not the smooth laminar BL where there is a steep shear layer very close to the wall which contributes significantly to the dissipation. In this case, the shear is very small in the valley region, but large around the tip (see figures 15 and 16). It is clearly seen that the shear rate in the region between the grooves is much less than that of the smooth case. Thus, it is reasonable that the dissipation from the BL contributes less and it is bulk dominant. We estimate the dissipation contributed from BL and bulk at two values of Taylor number from figure 23. At $Ta = 4.77 \times 10^7$, the region below the groove height contributes 49 % of the total dissipation while the bulk contributes 51 %. In contrast, at $Ta = 9.75 \times 10^8$, the region below the groove height contributes 65 % of the total dissipation while the bulk contributes 35 %. Therefore, according to the GL theory (Grossmann & Lohse 2000), in the regime close to $Ta = 4.77 \times 10^7$, where it is more bulk dominant, the local effective scaling exponent is larger than 0.38.

6. Conclusions

In this study, direct numerical simulations are conducted to explore Taylor–Couette flow in the presence of grooved walls. Numerical results corresponding to Taylor numbers up to $Ta = 2.15 \times 10^9$ are presented for three different sizes of groove, namely $\delta = 0.052d$, $\delta = 0.105d$ and $\delta = 0.209d$, at a radius ratio $\eta = 0.714$.

We find three different characteristic regimes, reflected in different effective scaling laws between Nu_ω and Ta. First, when $Ta < Ta_{th}$, i.e. when the boundary layer thickness is larger than the height of the grooves, there is an overlap regime in which smooth and groove cases show the same behaviour. Second, when $Ta > Ta_{th}$, i.e. when the boundary layer thickness is less than the groove height, there is a steep-slope regime in which the power-law exponent between Nu_ω and Ta becomes larger than the ultimate region effective scaling of 0.38. Third, when Ta is large enough, there is a saturation regime in which the effective scaling law saturates back to 0.38. It is found that, even after saturation, the slope is the same as for the smooth case, and the absolute value of torque is increased beyond the ratio of the surface area increase between grooved and smooth walls.

The visualization of the flow structure shows that the enhanced transport is caused by plume ejection from the tips of the grooves. First, the axial flow induces secondary vortices inside the grooves. Second, the interaction between the secondary vortices and the Taylor vortices facilitates flow separation on the tips. Third, this flow separation causes the boundary layer to detach into the bulk, and thus the boundary layer flow forms plumes and follows the preferential direction of Taylor vortices. Finally, the combination of plumes and flow separation greatly strengthens the convective part of Nu_ω. In particular, there is a possibility that the torque can become smaller when there are no plumes ejected from the tips of the grooves and the grooves impede the Taylor rolls. Another interesting feature revealed from visualizations is that large-scale Taylor vortices still survive in the presence of the grooves. This is because the induced secondary vortices inside the grooves also favour the circulation of the Taylor rolls.

With increasing Ta, the intensity of the secondary vortex inside the grooves is strengthened. The boundary layer thickness in the valley is decreased and more uniformly distributed along the surface of the groove. A small flat bulk region for the mean velocity profile can be seen inside the grooves. At high Ta, the azimuthal velocity cannot feel the effect of the grooves, and thus forms the uniformly thick BL, just as the smooth case. As to the fluctuation, it is found that, on the tips of the grooves, there is only one peak for the root mean square azimuthal velocity, while in the valley there are two peaks. The first peak is associated with the BL near the valley, and the second peak with the shear layer between the secondary vortices and the Taylor vortices. We found that the steep-slope regime is more bulk dominant, and therefore the effective scaling slope is larger, while in the saturation regime, the boundary layer contribution reoccurs, and hence the scaling slope saturates.

Our ambition is to further understand plume-triggered transitions. Ostilla-Mónico *et al.* (2014*a*) and van der Poel *et al.* (2015*b*) have shown that in smooth TC and RB flows the transition to the ultimate regime can be triggered by plumes because the regions of BLs where the plumes are ejected become turbulent. On the one hand, we would like to study whether in the grooved case the turbulent boundary layer can not only be formed on the tips of grooves, but for much larger Ta also inside the grooves, and thus lead to the ultimate regime. On the other hand, grooves can be used to manipulate the plumes because they are ejected from the tips of the grooves. If we implemented more and more grooves, and made the tips sharp enough such that there were more and more tips where plumes could be ejected, the ultimate regime could possibly be achieved at a much smaller Ta.

Acknowledgements

REFERENCES

AHLERS, G., GROSSMANN, S. & LOHSE, D. 2009 Heat transfer and large scale dynamics in turbulent Rayleigh–Bénard convection. *Rev. Mod. Phys.* **81**, 503–537.

VAN DEN BERG, T., DOERING, C., LOHSE, D. & LATHROP, D. 2003 Smooth and rough boundaries in turbulent Taylor–Couette flow. *Phys. Rev.* E **68**, 036307.

BRAUCKMANN, H. J. & ECKHARDT, B. 2013 Direct numerical simulations of local and global torque in Taylor–Couette flow up to $Re = 30\,000$. *J. Fluid Mech.* **718**, 398–427.

CADOT, O., COUDER, Y., DAERR, A., DOUADY, S. & TSINOBER, A. 1997 Energy injection in closed turbulent flows: stirring through boundary layers versus inertial stirring. *Phys. Rev.* E **56**, 427–433.

CHOI, H., MOIN, P. & KIM, J. 1993 Direct numerical simulation of turbulent flow over riblets. *J. Fluid Mech.* **255**, 503–539.

CHU, D. C. & KARNIADAKIS, G. E. 1993 Adirect numerical simulation of laminar and turbulent flow over riblet-mounted surfaces. *J. Fluid Mech.* **250**, 1–42.

CILIBERTO, S. & LAROCHE, C. 1999 Random roughness of boundary increases the turbulent scaling exponents. *Phys. Rev. Lett.* **82**, 3998–4001.

DU, Y.-B. & TONG, P. 2000 Turbulent thermal convection in a cell with ordered rough boundaries. *J. Fluid Mech.* **407**, 57–84.

ECKHARDT, B., GROSSMANN, S. & LOHSE, D. 2007a Fluxes and energy dissipation in thermal convection and shear flows. *Europhys. Lett.* **78**, 24001.

ECKHARDT, B., GROSSMANN, S. & LOHSE, D. 2007b Torque scaling in turbulent Taylor–Couette flow between independently rotating cylinders. *J. Fluid Mech.* **581**, 221–250.

FADLUN, E. A., VERZICCO, R., ORLANDI, P. & MOHD-YUSOF, J. 2000 Combined immersed-boundary finite-difference methods for three-dimensional complex flow simulations. *J. Comput. Phys.* **161**, 35–60.

FARDIN, M. A., PERGE, C. & TABERLET, N. 2014 'The hydrogen atom of fluid dynamics' – introduction to the Taylor–Couette flow for soft matter scientists. *Soft Matt.* **10**, 3523–3535.

VAN GILS, D. P. M., HUISMAN, S. G., BRUGGERT, G.-W., SUN, C. & LOHSE, D. 2011 Torque scaling in turbulent Taylor–Couette flow with co- and counterrotating cylinders. *Phys. Rev. Lett.* **106**, 024502.

GROSSMANN, S. & LOHSE, D. 2000 Scaling in thermal convection: a unifying theory. *J. Fluid Mech.* **407**, 27–56.

GROSSMANN, S. & LOHSE, D. 2001 Thermal convection for large Prandtl numbers. *Phys. Rev. Lett.* **86**, 3316–3319.

GROSSMANN, S. & LOHSE, D. 2002 Prandtl and Rayleigh number dependence of the Reynolds number in turbulent thermal convection. *Phys. Rev.* E **66**, 016301.

GROSSMANN, S. & LOHSE, D. 2011 Multiple scaling in the ultimate regime of thermal convection. *Phys. Fluids* **23**, 045108.

GROSSMANN, S. & LOHSE, D. 2012 Logarithmic temperature profiles in the ultimate regime of thermal convection. *Phys. Fluids* **24**, 125103.

GROSSMANN, S., LOHSE, D. & SUN, C. 2014 Velocity profiles in strongly turbulent Taylor–Couette flow. *Phys. Fluids* **26**, 025114.

GROSSMANN, S., LOHSE, D. & SUN, C. 2016 High Reynolds number Taylor–Couette flow. *Annu. Rev. Fluid Mech.* **48**, 53–80.

HE, X., FUNFSCHILLING, D., BODENSCHATZ, E. & AHLERS, G. 2012a Heat transport by turbulent Rayleigh–Bénard convection for $Pr \simeq 0.8$ and $4 \times 10^{11} \lesssim Ra \lesssim 2 \times 10^{14}$: ultimate-state transition for aspect ratio $\Gamma = 1.00$. *New J. Phys.* **14**, 063030.

HE, X., FUNFSCHILLING, D., NOBACH, H., BODENSCHATZ, E. & AHLERS, G. 2012b Transition to the ultimate state of turbulent Rayleigh–Bénard convection. *Phys. Rev. Lett.* **108**, 024502.

HUISMAN, S. G., VAN GILS, D. P. M., GROSSMANN, S., SUN, C. & LOHSE, D. 2012 Ultimate turbulent Taylor–Couette flow. *Phys. Rev. Lett.* **108**, 024501.

HUISMAN, S. G., SCHARNOWSKI, S., CIERPKA, C., KÄHLER, C. J., LOHSE, D. & SUN, C. 2013 Logarithmic boundary layers in strong Taylor–Couette turbulence. *Phys. Rev. Lett.* **110**, 264501.

JIMENEZ, J. 2004 Turbulent flows over rough walls. *Annu. Rev. Fluid Mech.* **36**, 173–196.

KRAICHNAN, R. H. 1962 Turbulent thermal convection at arbritrary Prandtl number. *Phys. Fluids* **5**, 1374–1389.

LATHROP, D. P., FINEBERG, J. & SWINNEY, H. L. 1992a Transition to shear-driven turbulence in Couette–Taylor flow. *Phys. Rev.* A **46**, 6390–6405.

LATHROP, D. P., FINEBERG, J. & SWINNEY, H. L. 1992b Turbulent flow between concentric rotating cylinders at large Reynolds number. *Phys. Rev. Lett.* **68**, 1515–1518.

LEWIS, G. S. & SWINNEY, H. L. 1999 Velocity structure functions, scaling, and transitions in high-Reynolds-number Couette–Taylor flow. *Phys. Rev.* E **59**, 5457–5467.

MARUSIC, I., MCKEON, B. J., MONKEWITZ, P. A., NAGIB, H. M., SMITS, A. J. & SREENIVASAN, K. R. 2010 Wall-bounded turbulent flows at high Reynolds numbers: recent advances and key issues. *Phys. Fluids.* **22** (6), 065103.

MITTAL, R. & IACCARINO, G. 2005 Immersed boundary methods. *Annu. Rev. Fluid. Mech.* **37**, 239–261.

NIKURADSE, J. 1933 Strömungsgesetze in rauhen Rohren. *Forschungsheft Arb. Ing.-Wes.* **361**.

OSTILLA, R., STEVENS, R. J. A. M., GROSSMANN, S., VERZICCO, R. & LOHSE, D. 2013 Optimal Taylor–Couette flow: direct numerical simulations. *J. Fluid Mech.* **719**, 14–46.

OSTILLA-MÓNICO, R., VAN DER POEL, E. P., VERZICCO, R., GROSSMANN, S. & LOHSE, D. 2014a Boundary layer dynamics at the transition between the classical and the ultimate regime of Taylor–Couette flow. *Phys. Fluids* **26**, 015114.

OSTILLA-MÓNICO, R., VAN DER POEL, E. P., VERZICCO, R., GROSSMANN, S. & LOHSE, D. 2014b Phase diagram of turbulent Taylor–Couette flow. *J. Fluid Mech.* **761**, 1–26.

VAN DER POEL, E. P., OSTILLA-MÓNICO, R., DONNERS, J. & VERZICCO, R. 2015a A pencil distributed code for simulating wall-bounded turbulent convection. *Comput. Fluids* **116**, 10–16.

VAN DER POEL, E. P., OSTILLA-MÓNICO, R., VERZICCO, R., GROSSMANN, S. & LOHSE, D. 2015b Logarithmic mean temperature profiles and their connection to plume emissions in turbulent Rayleigh–Bénard convection. *Phys. Rev. Lett.* **115**, 154501.

POPE, S. B. 2002 Wall flows. In *Turbulent Flows*, Cambridge Univerisity Press.

QIU, X.-L., XIA, K.-Q. & TONG, P. 2005 Experimental study of velocity boundary layer near a rough conducting surface in turbulent natural convection. *J. Turbul.* **6**, 1–13.

ROCHE, P.-E., CASTAING, B., CHABAUD, B. & HÉBRAL, B. 2001 Observation of the 1/2 power law in Rayleigh–Bénard convection. *Phys. Rev.* E **63**, 045303(R).

SALORT, J., LIOT, O., RUSAOUEN, E., SEYCHELLES, F., TISSERAND, J. C., CREYSSELS, M., CASTAING, B. & CHILLÀ, F. 2014 Thermal boundary layer near roughnesses in turbulent Rayleigh–Bénard convection: flow structure and multistability. *Phys. Fluids* **26**, 015112.

SHEN, Y., TONG, P. & XIA, K.-Q. 1996 Turbulent convection over rough surfaces. *Phys. Rev. Lett.* **76**, 908–911.

SMITS, A. J., MCKEON, B. J. & MARUSIC, I. 2011 High-Reynolds number wall turbulence. *Annu. Rev. Fluid. Mech.* **43** (1), 353–375.

STRINGANO, G., PASCAZIO, G. & VERZICCO, R. 2006 Turbulent thermal convection over grooved plates. *J. Fluid Mech.* **557**, 307–336.

TISSERAND, J. C., CREYSSELS, M., GASTEUIL, Y., PABIOU, H., GIBERT, M., CASTAING, B. & CHILLÀ, F. 2011 Comparison between rough and smooth plates within the same Rayleigh–Bénard cell. *Phys. Fluids* **23**, 015105.

VERZICCO, R. & ORLANDI, P. 1996 A finite-difference scheme for three-dimensional incompressible flows in cylindrical coordinates. *J. Comput. Phys.* **123**, 402–413.

WEI, P., CHAN, T.-S., NI, R., ZHAO, X.-Z. & XIA, K.-Q. 2014 Heat transport properties of plates with smooth and rough surfaces in turbulent thermal convection. *J. Fluid Mech.* **740**, 28–46.